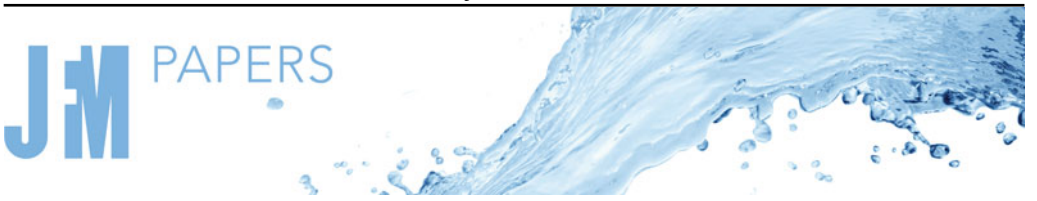
J. Fluid Mech. (2026), *vol.* 1037, A12, doi:10.1017/jfm.2026.11636



Lattice Boltzmann model for non-ideal compressible fluid dynamics

Seyed Ali Hosseini[1], **Milo Feinberg**[1] **and Ilya Karlin**[1]

[1]Department of Mechanical and Process Engineering, ETH Zurich, Zurich 8092, Switzerland

Corresponding authors: Ilya Karlin, karlin@lav.mavt.ethz.ch; Seyed Ali Hosseini, shosseini@ethz.ch; Milo Feinberg, mfeinberg@ethz.ch

(Received 16 October 2025 UTC; revised 11 March 2026 UTC; accepted 29 April 2026 UTC)

We present a new kinetic model and its lattice Boltzmann realisation for the simulation of compressible, non-ideal fluid flows. The method employs first-neighbour lattices and introduces a consistent set of correction terms constructed via quasi-equilibrium attractors, ensuring positive-definite and Galilean-invariant Navier–Stokes dissipation rates. This construction circumvents the need for extended stencils or *ad hoc* regularisation, while maintaining numerical stability and thermodynamic consistency across a broad range of flow regimes. The resulting model accurately reproduces both the Euler and Navier–Stokes hydrodynamic limits. As a stringent validation, we demonstrate, for the first time within a lattice Boltzmann framework, quantitatively accurate simulations of shock–drop interactions at Mach numbers up to 1.47. The proposed approach thus extends the applicability of lattice Boltzmann methods to high-speed, non-ideal compressible flows with a minimal kinetic stencil.

Key words: computational methods, gas/liquid flow, kinetic theory

1. Introduction

Non-ideal compressible fluid dynamics is a novel and rapidly developing branch of fluid mechanics, mainly due to the emergence of methods and technologies operating in the near-, trans- and super-critical regimes. It is, in part, concerned with the gas dynamics of single-phase fluids in non-ideal thermodynamic states, i.e. states where the compressibility factor differs from unity (Guardone *et al.* 2024). These states are illustrated in a pressure–temperature diagram for CO_2 in figure 1. Non-ideal compressible fluid dynamics encompasses the dynamics of supercritical fluids, dense vapours and liquids. The latter two are separated by the Widom line, an extension beyond the critical point that

© The Author(s), 2026. Published by Cambridge University Press. This is an Open Access article, distributed under the terms of the Creative Commons Attribution licence (https://creativecommons.org/licenses/by/4.0/), which permits unrestricted re-use, distribution and reproduction, provided the original article is properly cited.

https://doi.org/10.1017/jfm.2026.11636 Published online by Cambridge University Press

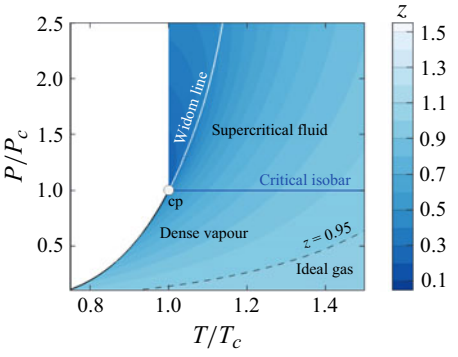


Figure 1. Pressure–temperature diagram for CO_2. The colour scale indicates the compressibility factor $Z = P/\rho RT$, where ρ, P and R are the density, pressure and specific gas constant, respectively. Figure reproduced from Guardone *et al.* (2024). Here, P_c and T_c are the critical pressure and temperature.

delineates vapour-like and liquid-like behaviours, identified by maxima in the constant-pressure specific heat (Simeoni *et al.* 2010). In addition, it includes fluids of higher molecular complexity with a negative fundamental derivative of gas dynamics (Colonna *et al.* 2009), also known as Bethe–Zel'dovich–Thompson (BZT) fluids (Zel'Dovich 1946; Thompson & Lambrakis 1973) as well as simple fluids in the proximity of the critical point. The rapidly growing interest within the energy industry in fluids operating in such thermodynamic states, together with their marked departure from ideal-gas behaviour, demonstrates the need for systematic studies of such flows. However, as evident in the literature, while considerable effort has been devoted to developing experimental set-ups for non-ideal fluid dynamics in recent years (Lettieri, Yang & Spakovszky 2015; Zocca *et al.* 2019; Gallarini *et al.* 2021; Head *et al.* 2022), experimental data remain scarce and are complicated to acquire (Guardone *et al.* 2024). Consequently, the development of consistent and efficient numerical tools for the simulation of such flows is essential for advancing both the fundamental understanding of non-ideal compressible fluid dynamics and technologies such as organic Rankine cycles and supercritical CO_2 turbines (Chen *et al.* 2023; Gunawan, Permana & Soetikno 2023; Guardone *et al.* 2024). More specifically, direct numerical simulations are necessary both to understand the complex physics of non-ideal compressible fluid dynamics and to generate engineering databases. Examples include skin friction and dissipation coefficients (Cramer, Whitlock & Tarkenton 1996; Pini & De Servi 2018), heat transfer in wall-bounded turbulent supercritical flows (Peeters *et al.* 2016; Kawai 2019) and the critical mass flow rate and pressure in nozzles and turbines involving flashing flows. While direct numerical simulations may at times be cost prohibitive for full-scale simulations, they are a necessary tool for the development of subgrid-scale closure models required for the more cost effective large eddy and Reynolds-averaged Navier–Stokes simulations (Garnier, Adams & Sagaut 2009). Recent studies on homogeneous isotropic turbulence fluid structures in dense vapours have shown that, while large-scale flow structures are mostly affected by molecular complexity, smaller-scale flow structures are impacted by local variations in sound speed (Sciacovelli, Cinnella & Grasso 2017; Duan *et al.* 2021). In addition, the dense vapour has been shown to display modified shocklet structures, with considerably reduced jumps in pressure, density and entropy in compression shocklets, and the emergence of expansion shocklets (Giauque *et al.* 2017, 2020). Similarly, substantial differences from ideal-gas dynamics have been reported (Vadrot, Giauque & Corre 2021) for wall-bounded turbulence, particularly at smaller scales, and where strong normal gradients in density and viscosity – and consequently

https://doi.org/10.1017/jfm.2026.11636 Published online by Cambridge University Press

the local speed of sound and Mach number – may strongly impact turbulent structures (Peeters *et al.* 2016; Pecnik & Patel 2017). Reliable direct numerical simulation studies of non-ideal compressible fluid dynamics can fill existing gaps in the understanding of physics of such flows. A reliable numerical scheme presupposes a physical model valid across all regimes of interest here, i.e. super-, trans- and near-critical flows involving pronounced non-ideal and compressibility effects. The development and validation of efficient numerical schemes for the Navier–Stokes–Korteweg (NSK) dynamics, regardless of method, can have a significant impact on the broader literature and understanding of non-ideal compressible flows.

The lattice Boltzmann method (LBM) is an excellent candidate for the flow regimes of interest here. Already well established as an efficient method for resolved simulation of flows in the incompressible limit, the distinct numerical features of LBM offer advantages for compressible, non-ideal fluid dynamics. Specifically, LBM benefits from the decoupling of nonlinearity and non-locality noted by S. Succi, in LBM 'nonlinearity is local, non-locality is linear' (Succi 2001; Succi & Succi 2018). The LBM solvers are conservative and low-dissipative schemes with spectral properties – both dissipative and dispersive – that compare favourably to conventional solvers of the same order (Martinez *et al.* 1994; Peng *et al.* 2010; Hosseini *et al.* 2019, 2022*b*; Wissocq, Sagaut & Boussuge 2019; Hosseini 2020), especially for normal propagation modes, i.e. acoustic modes (Bres, Pérot & Freed 2009; Viggen 2011, 2014). Along with incompressible ideal fluid dynamics, two-phase flow simulation has witnessed major success and growth in popularity in LBM, starting with formulations such as the colour gradient (Gunstensen *et al.* 1991), pseudo-potential (Shan & Chen 1993) and free energy (Swift *et al.* 1996) in the early 1990s. The latter two are of special interest in the context of non-ideal fluid dynamics as they effectively solve a form of the NSK. The vast majority of the literature that focuses on or uses this class of models has been tailored to become essentially highly efficient interface tracking models for multi-phase flows (Chen *et al.* 2014; Mazloomi, Chikatamarla & Karlin 2015; Li *et al.* 2016; Luo, Fei & Wang 2021; Hosseini & Karlin 2023). Non-ideal compressible thermodynamics has long been neglected in LBM applications. The free energy model, for instance, which is the only one out of the previously listed approaches that results from minimisation of a free energy functional under a constraint on the total mass, can readily be shown to be related to mean-field kinetic models such as the Boltzmann–Enskog–Vlasov (Hosseini *et al.* 2022*a*; Hosseini & Karlin 2023) equations and recover, in the hydrodynamic limit and under specific scaling, the NSK equations (Hosseini *et al.* 2022*a*) and mean-field van der Waals fluid thermodynamics. This means that it can not only model two-phase flow dynamics and phase separation but also properly recover all mean-field, near-, trans- and super-critical behaviours associated with non-ideal fluids, as demonstrated, for instance, through studies of properties such as the Tollman length (Házi & Márkus 2008; Reyhanian *et al.* 2020, 2021; Hosseini *et al.* 2022*a*; Lulli *et al.* 2022*a*,*b*; Hosseini & Karlin 2023).

The use and extension of this class of thermodynamically consistent models to compressible non-ideal fluid dynamics is a largely under-explored area that can considerably impact research on non-ideal compressible fluid dynamics. Early attempts at developing an LBM for compressible non-ideal flows were documented in He & Doolen (2002). Since then, thermal multi-phase models based on the pseudo-potential approach have witnessed steady growth. However, the vast majority of the models and studies in the literature have been tailored to boiling applications (see for instance Li *et al.* 2015; Fang *et al.* 2017; Fei *et al.* 2020; Huang, Wu & Adams 2021; Saito *et al.* 2021). To the authors' knowledge, the only documented attempts at modelling compressible non-ideal flows beyond evaporation are Vienne, Giauque & Lévêque (2024), where a

https://doi.org/10.1017/jfm.2026.11636 Published online by Cambridge University Press

hybrid lattice Boltzmann/finite-volume scheme – with a finite-volume discretisation of the energy equation – was proposed, and Reyhanian *et al.* (2020, 2021), where the authors demonstrated a numerical model based on the particles-on-demand realisation of the LBM (Dorschner, Bösch & Karlin 2018). We propose to address this gap in the literature with a novel kinetic model and its lattice Boltzmann realisation for non-ideal fluids in the compressible regime. To retain the main advantages of the LBM, the proposed model relies on classical first-neighbour lattices, taking advantage of a second distribution function for the energy-balance equation (Rykov 1975; Prasianakis & Karlin 2007, 2008; Saadat *et al.* 2021*b*). The kinetic model relies on a novel set of Bhatnagar-Gross-Krook (BGK)-like collision operators with local- and shifted-equilibrium attractors, ensuring recovery of the target hydrodynamics. For instance, independent control over the bulk viscosity is guaranteed through the shifted equilibrium; the latter is a critical point as the bulk viscosity dictated by the BGK structure, for equilibria with pressures other than the ideal-gas pressure, can take on negative values in the hydrodynamic limit; see Hosseini *et al.* (2022*a*). Together with a consistent second-order discretisation and treatment of source terms, the model will be shown to correctly recover the target hydrodynamic limit.

The paper is organised as follows: § 2 introduces the target hydrodynamic limit. Section 3 presents the kinetic model and its lattice Boltzmann realisation. Section 4 provides validation across a range of increasingly complex configurations and studies of non-ideal fluid-specific dynamics through cases such as shock tubes and shock–liquid-column interaction. The article closes with final remarks in § 5.

2. Balance equations for a compressible non-ideal fluid

We begin with a brief overview of a one-component, compressible non-ideal fluid system. Material presented in this section is standard and serves to define the target hydrodynamics for a kinetic model to be introduced in § 3. We introduce the macroscopic fields of fluid density $\rho(\boldsymbol{x}, t)$, momentum $\rho\boldsymbol{u}(\boldsymbol{x}, t)$, where $\boldsymbol{u}(\boldsymbol{x}, t)$ is the fluid velocity vector, and bulk energy $\rho E(\boldsymbol{x}, t)$. The latter is the sum of the flow kinetic-energy density and the internal-energy density ρe

$$\rho E = \rho e + \frac{1}{2}\rho u^2. \tag{2.1}$$

The specific internal-energy $e(v, T)$ per unit mass is a function of absolute temperature T and specific volume $v = 1/\rho$, and is defined by a familiar thermodynamic relation for its differential

$$\mathrm{d}e = c_v\,\mathrm{d}T + \left[T\left(\frac{\partial P}{\partial T}\right)_v - P\right]\mathrm{d}v, \tag{2.2}$$

where $P(v, T)$ is the thermodynamic pressure and c_v is the specific heat at constant volume

$$c_v = \left(\frac{\partial e}{\partial T}\right)_v. \tag{2.3}$$

In the following, it will be convenient to consider the thermodynamic equation of state as a function of the density ρ rather than of the specific volume v

$$P(\rho, T) = P(v, T)|_{v=1/\rho}\,, \tag{2.4}$$

so that the differential of the internal energy (2.2) becomes

$$\mathrm{d}e = c_v\mathrm{d}T - \left[T\left(\frac{\partial P}{\partial T}\right)_\rho - P\right]\frac{\mathrm{d}\rho}{\rho^2}. \tag{2.5}$$

https://doi.org/10.1017/jfm.2026.11636 Published online by Cambridge University Press

The mass, momentum and bulk-energy-balance equations are

$$\partial_t \rho + \nabla \cdot \rho \boldsymbol{u} = 0, \tag{2.6}$$

$$\partial_t (\rho \boldsymbol{u}) + \nabla \cdot \rho \boldsymbol{u} \otimes \boldsymbol{u} + \nabla P + \nabla \cdot \boldsymbol{T}_{NS} + \nabla \cdot \boldsymbol{T}_K = 0, \tag{2.7}$$

$$\partial_t (\rho E) + \nabla \cdot (\rho E \boldsymbol{u} + P \boldsymbol{u}) + \boldsymbol{u} \cdot (\nabla \cdot \boldsymbol{T}_K) + \nabla \cdot (\boldsymbol{u} \cdot \boldsymbol{T}_{NS}) + \nabla \cdot \boldsymbol{q}_F = 0. \tag{2.8}$$

The viscous stress tensor is defined as

$$\boldsymbol{T}_{NS} = -\mu \left(\nabla \boldsymbol{u} + \nabla \boldsymbol{u}^\dagger - \frac{2}{D} (\nabla \cdot \boldsymbol{u}) \boldsymbol{I} \right) - \eta (\nabla \cdot \boldsymbol{u}) \boldsymbol{I}, \tag{2.9}$$

where μ and η are the dynamic shear and bulk viscosity coefficients, respectively. Furthermore, the Korteweg surface tension tensor is defined as

$$\boldsymbol{T}_K = \kappa \nabla \rho \otimes \nabla \rho - \kappa \left(\rho (\nabla \cdot \nabla) \rho + \frac{1}{2} |\nabla \rho|^2 \right) \boldsymbol{I}, \tag{2.10}$$

where κ is the capillarity coefficient. Since only the divergence of Korteweg's tensor contributes to the balance equations, we define the Korteweg force as

$$\boldsymbol{F} = -\nabla \cdot \boldsymbol{T}_K = \kappa \rho \nabla (\nabla \cdot \nabla) \rho. \tag{2.11}$$

Finally, the Fourier heat flux is defined as

$$\boldsymbol{q}_F = -k \nabla T, \tag{2.12}$$

where k is the thermal conductivity coefficient. All transport coefficients are considered constants below.

While the bulk-energy balance (2.8) is our primary target equation in the following, we mention several other related forms that are implied by the system (2.6), (2.7) and (2.8). Denoting by $\mathcal{K} = (1/2)\rho u^2$ the flow kinetic energy, and computing its time derivative using the continuity (2.6) and the momentum balance (2.7), we obtain

$$\partial_t \mathcal{K} + \nabla \cdot (\mathcal{K} \boldsymbol{u}) = -\boldsymbol{u} \cdot \nabla P - (\boldsymbol{u} \nabla) : \boldsymbol{T}_K - (\boldsymbol{u} \nabla) : \boldsymbol{T}_{NS}. \tag{2.13}$$

Using the decomposition (2.1), the internal-energy balance is obtained by subtracting the kinetic-energy balance (2.13) from the bulk-energy balance (2.8)

$$\rho (\partial_t e + \boldsymbol{u} \cdot \nabla e) = -P (\nabla \cdot \boldsymbol{u}) - \boldsymbol{T}_{NS} : \nabla \boldsymbol{u} - \nabla \cdot \boldsymbol{q}_F. \tag{2.14}$$

Furthermore, using the differential of the internal energy (2.5) and the continuity (2.6), one obtains the temperature equation

$$\rho c_v (\partial_t T + \boldsymbol{u} \cdot \nabla T) = -T \left(\frac{\partial P}{\partial T} \right)_\rho (\nabla \cdot \boldsymbol{u}) - \boldsymbol{T}_{NS} : \nabla \boldsymbol{u} - \nabla \cdot \boldsymbol{q}_F, \tag{2.15}$$

and similarly, the pressure equation

$$\partial_t P + \boldsymbol{u} \cdot \nabla P = -\rho c_s^2 (\nabla \cdot \boldsymbol{u}) - \frac{1}{\rho c_v} \left(\frac{\partial P}{\partial T} \right)_\rho (\boldsymbol{T}_{NS} : \nabla \boldsymbol{u} + \nabla \cdot \boldsymbol{q}_F), \tag{2.16}$$

where c_s is the speed of sound

$$c_s^2 = \left(\frac{\partial P}{\partial \rho} \right)_T + \frac{T}{\rho^2 c_v} \left(\frac{\partial P}{\partial T} \right)_\rho^2. \tag{2.17}$$

A further useful form is the balance for the total energy $\mathcal{E}$, which takes into account the energy of the liquid–vapour interface

$$\mathcal{E} = \rho E + \frac{1}{2} \kappa |\nabla \rho|^2. \tag{2.18}$$

https://doi.org/10.1017/jfm.2026.11636 Published online by Cambridge University Press

Introducing the interface energy, $\mathcal{E}_\kappa = (1/2)\kappa|\nabla\rho|^2$, we first compute its time derivative using the continuity (2.6) to get

$$\partial_t \mathcal{E}_\kappa + \nabla\cdot(\mathcal{E}_\kappa \boldsymbol{u}) + \boldsymbol{T}_K : \nabla\boldsymbol{u} + \nabla\cdot(\kappa\rho(\nabla\cdot\boldsymbol{u})\nabla\rho) = 0. \tag{2.19}$$

Adding the bulk-energy balance (2.8) and the interface-energy balance (2.19), we obtain the balance equation for the total energy (2.18) in the standard form

$$\partial_t \mathcal{E} + \nabla\cdot\left(\mathcal{E}\boldsymbol{u} + P\boldsymbol{u} + \boldsymbol{T}_{NS}\cdot\boldsymbol{u} + \boldsymbol{T}_K\cdot\boldsymbol{u} + \kappa\rho(\nabla\cdot\boldsymbol{u})\nabla\rho + \boldsymbol{q}_F\right) = 0. \tag{2.20}$$

In summary, the various energy-balance forms listed above are implied by the set of balance equations for mass (2.6), momentum (2.7) and bulk energy (2.8), which constitute the target equations for the lattice Boltzmann realisation. While the total energy-balance form (2.20) seems to be preferred for conventional finite-volume methods, the bulk-energy version of the energy balance is more convenient in the lattice Boltzmann setting due to the locality of the corresponding bulk-energy field.

Furthermore, we mention a special case in which the specific heat at constant volume is a function of the absolute temperature only, $c_v = c_v(T)$. This implies that the thermodynamic equation of state is a linear function of temperature

$$P(v, T) = Tb(v) + a(v), \tag{2.21}$$

where a and b are functions of specific volume (or density) only. Indeed, since (2.2) is a complete differential, the equality of mixed derivatives implies

$$\frac{\partial c_v}{\partial v} = \frac{\partial}{\partial T}\left[T\left(\frac{\partial P}{\partial T}\right) - P\right] = T\frac{\partial^2 P}{\partial T^2} = 0. \tag{2.22}$$

Commonly used examples are the van der Waals and the Carnahan–Starling equations of state. From a more microscopic viewpoint, corresponding balance equations are derived from the Enskog–Vlasov kinetic equation. To link the aforementioned energy equations to those appearing in the kinetic theory, we decompose the pressure into hard-sphere and mean-field contributions. We define the excluded volume, or Enskog, contributions as $P_{hs} = TB(\rho) = Tb(1/\rho)$, and the mean-field, or Vlasov, contributions as $P_{mf} = A(\rho) = a(1/\rho)$. This permits the above equation of state (2.21) to be written

$$P = P_{hs} + P_{mf}. \tag{2.23}$$

The specific internal energy is partitioned accordingly

$$\mathrm{d}e = \mathrm{d}e_{hs} + \mathrm{d}e_{mf}, \tag{2.24}$$

$$\mathrm{d}e_{hs} = c_v(T)\mathrm{d}T, \tag{2.25}$$

$$\mathrm{d}e_{mf} = P_{mf}\frac{\mathrm{d}\rho}{\rho^2}. \tag{2.26}$$

Here, e_{hs} is the specific thermal energy, and e_{mf} is the specific molecular potential energy (in the mean-field approximation). For the Enskog model of hard spheres, the specific heat is that of the ideal monatomic gas, $c_v = (3/2)R$. The balance equation for the thermal energy ρe_{hs} is obtained by excluding the molecular potential energy from the balance of the internal energy (2.14)

$$\partial_t(\rho e_{hs}) + \nabla\cdot(\rho e_{hs}\boldsymbol{u}) + P_{hs}(\nabla\cdot\boldsymbol{u}) + \boldsymbol{T}_{NS} : \nabla\boldsymbol{u} + \nabla\cdot\boldsymbol{q}_F = 0. \tag{2.27}$$

Introducing the total kinetic energy of hard spheres

$$\rho E_{hs} = \rho e_{hs} + \frac{1}{2}\rho u^2, \tag{2.28}$$

https://doi.org/10.1017/jfm.2026.11636 Published online by Cambridge University Press

we obtain its balance upon adding the flow kinetic energy (2.13) to the thermal energy balance (2.27)

$$\partial_t(\rho E_{hs}) + \boldsymbol{\nabla}\cdot(\rho E_{hs}\boldsymbol{u} + P_{hs}\boldsymbol{u}) + \boldsymbol{u}\cdot\left(\boldsymbol{\nabla} P_{mf} + \boldsymbol{\nabla}\cdot\boldsymbol{T}_K\right) + \boldsymbol{\nabla}\cdot(\boldsymbol{u}\cdot\boldsymbol{T}_{NS}) + \boldsymbol{\nabla}\cdot\boldsymbol{q}_F = 0. \tag{2.29}$$

The balance (2.29) can be derived directly from the Enskog–Vlasov kinetic equation under appropriate scaling in the hydrodynamic limit. Conversely, starting with the energy balance (2.29) and adding the balance for the potential energy (2.26) (since e_{mf} depends only on the density, the latter follows from the continuity equation)

$$\partial_t(\rho e_{mf}) + \boldsymbol{\nabla}\cdot\left(\rho e_{mf}\boldsymbol{u} + P_{mf}\boldsymbol{u}\right) - \boldsymbol{u}\cdot\boldsymbol{\nabla} P_{mf} = 0, \tag{2.30}$$

we recover the bulk-energy balance (2.8) (and, consequently, after adding the balance of the interface energy (2.19), the total energy balance (2.20)), for the special case of the equation of state (2.21). These considerations show that a more general phenomenological bulk-energy balance (2.8) is consistent with the special case derived directly from kinetic theory and thus gives us a further reason to use (2.8) as the target energy-balance equation in the lattice Boltzmann context. Consequently, and without loss of generality, we use the van der Waals equation of state in the numerical examples below

$$P(\rho, T) = \frac{\rho RT}{1 - b\rho} - a\rho^2. \tag{2.31}$$

The excluded volume parameter b and the long-range molecular attraction parameter a are defined in terms of the critical-state thermodynamic data, the critical density ρ_c, critical temperature T_c and critical pressure P_c, as follows: $a = 27R^2T_c^2/64P_c$, $b = RT_c/8P_c$. The differentials of the specific internal energy (2.5) and of the specific entropy s for the van der Waals fluid are, respectively,

$$\mathrm{d}e = c_v\,\mathrm{d}T - a\,\mathrm{d}\rho, \tag{2.32}$$

$$\mathrm{d}s = \frac{c_v}{T}\,\mathrm{d}T - \frac{R}{\rho(1 - b\rho)}\,\mathrm{d}\rho. \tag{2.33}$$

In the next section, we shall introduce a lattice Boltzmann model that recovers the above system of balance (2.6), (2.7) and (2.8) in the hydrodynamic limit. Before doing so, we highlight a motivation for adopting the lattice Boltzmann formulation for modelling compressible non-ideal fluids. From the pressure (2.16), one observes that, for a non-ideal fluid, the adiabatic speed of sound squared (2.17) becomes negative for a van der Waals-type equation of state in the thermodynamically unstable spinodal region of the density–temperature diagram. Consequently, in the inviscid limit, the evolution equation changes type from hyperbolic to elliptic, and special treatment invoking Maxwell's equal-area rule has to be applied in conventional computational fluid dynamics methods. In contrast, the LBM, by being based in kinetic theory, is able to circumvent this issue as it inherits propagation along fixed characteristics, namely the discrete velocities. Thus, the lattice Boltzmann model introduced below should not be viewed as yet another interface-capturing numerical scheme for multiphase flows but rather as a reduced kinetic theory targeting the thermodynamically consistent compressible NSK hydrodynamic limit.

3. Lattice Boltzmann model for non-ideal compressible flows

3.1. *Kinetic model*

In this section, we introduce a kinetic model tailored to recover the target hydrodynamic equations of a compressible non-ideal fluid, (2.6), (2.7) and (2.8), in the hydrodynamic

https://doi.org/10.1017/jfm.2026.11636 Published online by Cambridge University Press

limit. To this end, we follow the so-called double distribution function approach and consider two velocity distribution functions, $f(\boldsymbol{v}, \boldsymbol{x}, t)$ and $g(\boldsymbol{v}, \boldsymbol{x}, t)$, where $\boldsymbol{v}$ is the velocity of a particle. The idea of a double distribution function kinetic model was first proposed by Rykov (1975) for polyatomic molecules, where the second distribution function represents the rotational–vibrational contribution to the internal energy. This approach was later adopted in the LBM (He, Chen & Doolen 1998; Guo *et al.* 2007; Li *et al.* 2007; Karlin, Sichau & Chikatamarla 2013), where the second distribution function has been used to represent different forms of energy. Here, we propose a model where the bulk energy ρE (2.1) is represented by the second distribution function, although other choices are possible. This specific choice leads to kinetic equations without complicated source terms and can be efficiently tackled by classical first-neighbour discrete-velocity lattices. We refer interested readers to Hosseini, Bhadauria & Karlin (2024) and Strässle *et al.* (2025) for an in-depth discussion.

Thus, the f-distribution function defines the fluid density and momentum, while the g-distribution defines the bulk energy (2.1)

$$\int \{m, m\boldsymbol{v}\} f \,\mathrm{d}\boldsymbol{v} = \{\rho, \rho\boldsymbol{u}\}, \tag{3.1}$$

$$\int m g \,\mathrm{d}\boldsymbol{v} = \rho E, \tag{3.2}$$

where m is the mass of the particle. The kinetic model is defined by the coupled kinetic equations

$$\partial_t f + \boldsymbol{v} \cdot \nabla f = \mathcal{F}, \tag{3.3}$$

$$\partial_t g + \boldsymbol{v} \cdot \nabla g = \mathcal{G}, \tag{3.4}$$

where the collision terms on the right-hand side are sought in the following forms:

$$\mathcal{F} = \frac{1}{\tau}\left(f^{eq} - f\right) + \frac{1}{\lambda}\left(f^{\star}_{\lambda} - f^{eq}\right), \tag{3.5}$$

$$\mathcal{G} = \frac{1}{\tau}\left(g^{eq} - g\right) + \frac{1}{\lambda}\left(g^{\star}_{\lambda} - g^{eq}\right). \tag{3.6}$$

Here, the pair $\{f^{eq}, g^{eq}\}$ represents a local-equilibrium attractor, while $\{f^{\star}_{\lambda}, g^{\star}_{\lambda}\}$ represents an intermediate quasi-equilibrium attractor. Furthermore, τ and λ are the corresponding relaxation times, and we proceed to define the equilibrium and the quasi-equilibrium distribution functions.

To describe the equilibrium distribution functions, we introduce a reference temperature parameter θ, with dimensions of RT. This parameter fixes the width of the Maxwellian equilibria independent of the thermodynamic internal energy. The equilibrium associated with mass and momentum is then written as

$$f^{eq}(\rho, \boldsymbol{u}, \theta) = \frac{\rho}{m(2\pi\theta)^{D/2}} \exp\left[-\frac{|\boldsymbol{v} - \boldsymbol{u}|^2}{2\theta}\right], \tag{3.7}$$

where ρ and the D components of $\boldsymbol{u}$ are fixed by the local conservation constraints (3.1), while θ is specified independently. Thus, f^{eq} forms a $D+2$-parameter family.

The equilibrium distribution associated with the energy population is defined as

$$g^{eq}(\rho, \boldsymbol{u}, T, \theta) = \left(\frac{\boldsymbol{v}^2}{2} + e(\rho, T) - \frac{D\theta}{2}\right) f^{eq}(\rho, \boldsymbol{u}, \theta), \tag{3.8}$$

so that the thermodynamic temperature T enters through the specific internal energy $e(\rho, T)$, whereas θ enters through the Maxwellian kernel. The equilibrium distributions

https://doi.org/10.1017/jfm.2026.11636 Published online by Cambridge University Press

(3.7) and (3.8) satisfy the conservation laws of mass, momentum and bulk energy

$$\int \{m, m\boldsymbol{v}\} f^{eq}\,\mathrm{d}\boldsymbol{v} = \{\rho, \rho\boldsymbol{u}\}, \tag{3.9}$$

$$\int m g^{eq}\,\mathrm{d}\boldsymbol{v} = \rho E. \tag{3.10}$$

Other relevant higher-order moments of the equilibrium distributions are presented in table 5 in Appendix A.

The quasi-equilibrium state $\{f_\lambda^\star, g_\lambda^\star\}$ is constructed using shifted values of the flow velocity, reference temperature and thermodynamic temperature

$$\boldsymbol{u}_\lambda^\star = \boldsymbol{u} + \lambda\frac{\boldsymbol{F}}{\rho}, \tag{3.11}$$

$$\theta_\lambda^\star = \theta + \lambda\alpha\theta\,(\boldsymbol{\nabla}\cdot\boldsymbol{u}), \tag{3.12}$$

$$T_\lambda^\star = T - \lambda^2\frac{\boldsymbol{F}\cdot\boldsymbol{F}}{2\rho^2 c_v}, \tag{3.13}$$

where $\boldsymbol{F}$ is the Korteweg force (2.11), and α is a non-dimensional parameter to be specified below. The quasi-equilibrium distribution $f_\lambda^\star$ therefore is a shifted Maxwellian

$$f_\lambda^\star(\rho, \boldsymbol{u}_\lambda^\star, \theta_\lambda^\star) = f^{eq}(\rho, \boldsymbol{u}_\lambda^\star, \theta_\lambda^\star). \tag{3.14}$$

The corresponding quasi-equilibrium for the energy population is defined as

$$g_\lambda^\star(\rho, \boldsymbol{u}_\lambda^\star, T_\lambda^\star, \theta_\lambda^\star) = \left(\frac{\boldsymbol{v}^2}{2} + e(\rho, T_\lambda^\star) - \frac{D\theta_\lambda^\star}{2} + \frac{\boldsymbol{q}_\lambda^c\cdot(\boldsymbol{v}-\boldsymbol{u})}{\rho\theta}\right) f^{eq}\left(\rho, \boldsymbol{u}_\lambda^\star, \theta_\lambda^\star\right). \tag{3.15}$$

The vector $\boldsymbol{q}_\lambda^c$ appearing in the last term is defined by

$$\boldsymbol{q}_\lambda^c = \lambda P\left(\boldsymbol{\nabla}h - \frac{k}{\mu}\boldsymbol{\nabla}T\right), \tag{3.16}$$

where h is the specific enthalpy:

$$h = e + \frac{P}{\rho}. \tag{3.17}$$

Moments of the quasi-equilibrium distributions $f_\lambda^\star$ (3.14) and $g_\lambda^\star$ (3.15) are presented in tables 5 and 6 in Appendix A.

The construction above leaves two scalar parameters to be specified: the reference temperature θ and the non-dimensional coefficient α in (3.12). To specify these free parameters, we perform a Chapman–Enskog analysis of the hydrodynamic limit of the kinetic equations. Details are given in Appendix A. The analysis shows that, to recover the target hydrodynamic set (2.6), (2.7) and (2.8), the reference temperature must be set as the thermodynamic flow work

$$\theta = \frac{P}{\rho}. \tag{3.18}$$

Recovery of the Navier–Stokes viscous stress tensor (2.9) requires the relaxation time τ be related to the shear viscosity μ as

$$\tau = \frac{\mu}{P}, \tag{3.19}$$

https://doi.org/10.1017/jfm.2026.11636 Published online by Cambridge University Press

and the parameter α to have the form

$$\alpha = \left(\frac{D+2}{D} - \frac{\rho c_s^2}{P} - \frac{\eta}{\mu} \right). \tag{3.20}$$

Note that the relaxation time λ does not affect the hydrodynamic limit, thus remaining a free parameter which can be specified conveniently in the subsequent discretisation. We close this section with several explanatory comments.

(i) In the ideal-gas limit, $P \to \rho RT$, the reference temperature (3.18) becomes proportional to the thermodynamic temperature, $\theta \to RT$. For a generic non-ideal compressible fluid, the formulation of the reference temperature (3.18), as a function of P and ρ, rather than thermodynamic temperature T, was first proposed by Reyhanian, Dorschner & Karlin (2020) in the context of the particles-on-demand method (Dorschner *et al.* 2018).

(ii) A special case of kinetic models (3.3) and (3.4) was recently derived from the Boltzmann–Enskog–Vlasov kinetic theory by Karlin & Hosseini (2026) using a projection operator technique. Here, we introduced a more general kinetic model, combining the aforementioned approach of Reyhanian *et al.* (2020) with the quasi-equilibrium representation of the non-local Korteweg force.

(iii) In the absence of the term (3.16), the non-equilibrium heat flux recovered in the hydrodynamic limit is proportional to the enthalpy gradient, $\boldsymbol{q} \propto \nabla h$, as first observed by Reyhanian *et al.* (2020). In the ideal-gas limit this reduces to Fourier's law (2.12), since $\nabla h \propto \nabla T$. For a general non-ideal fluid, however, ∇h also contains density-gradient contributions, leading to a spurious non-Fourier component of the heat flux. The correction flux (3.16) compensates for this non-Fourier contribution, thereby recovering (2.12).

(iv) Setting $\alpha = 0$ in (3.12) recovers a fixed bulk viscosity $\eta = \mu(((D+2)/D) - (\rho c_s^2/P))$. Shifting the reference temperature with the parameter α (3.20) renders the bulk viscosity an independent, tuneable and positive-definite parameter.

(v) From the Chapman–Enskog analysis, the zeroth moment of $g_\lambda^\star$

$$\int m g_\lambda^\star \mathrm{d}\boldsymbol{v} = \frac{1}{2}\rho \boldsymbol{u}^2 + \lambda \boldsymbol{u} \cdot \boldsymbol{F} + \frac{\lambda^2}{2\rho} \boldsymbol{F} \cdot \boldsymbol{F} + \rho e(\rho, T_\lambda^\star), \tag{3.21}$$

must differ from the corresponding moment of g^{eq} only by the term $\lambda \boldsymbol{u} \cdot \boldsymbol{F}$. The additional kinetic energy introduced by the shifted velocity $\boldsymbol{u}_\lambda^\star$ must therefore be compensated by a commensurate reduction in the internal energy. Introducing $\delta T = T_\lambda^\star - T$, we can expand

$$e(\rho, T_\lambda^\star) = e(\rho, T) + \left. \frac{\partial e}{\partial T} \right|_\rho \delta T + \mathcal{O}\left(\delta T^2\right). \tag{3.22}$$

To recover the correct moment up to order λ^2, one therefore requires

$$\left. \frac{\partial e}{\partial T} \right|_\rho \delta T = -\frac{\lambda^2}{2\rho^2} \boldsymbol{F} \cdot \boldsymbol{F}. \tag{3.23}$$

This yields the expression (3.13) for the shifted temperature. Since $.\partial e/\partial T|_\rho = c_v > 0$, the shifted temperature $T_\lambda^\star$ is systematically lower than T.

(vi) The role of the quasi-equilibrium state can be clarified by considering the limit $\lambda \to 0$, in which relaxation toward the shifted state becomes equivalent to introducing explicit kinetic source terms

https://doi.org/10.1017/jfm.2026.11636 Published online by Cambridge University Press

$$\lim_{\lambda\to 0}\frac{1}{\lambda}(f_\lambda^\star - f^{eq}) = \frac{1}{P}\boldsymbol{F}\cdot(\boldsymbol{v}-\boldsymbol{u})f^{eq} + \alpha(\boldsymbol{\nabla}\cdot\boldsymbol{u})\left(\frac{\rho(\boldsymbol{v}-\boldsymbol{u})^2}{2P} - \frac{D}{2}\right)f^{eq}, \tag{3.24}$$

$$\begin{aligned}\lim_{\lambda\to 0}\frac{1}{\lambda}(g_\lambda^\star - g^{eq}) = {}& \frac{1}{P}\boldsymbol{F}\cdot(\boldsymbol{v}-\boldsymbol{u})\left(\frac{\boldsymbol{v}^2}{2} + e - \frac{DP}{2\rho}\right)f^{eq} \\ & + \alpha(\boldsymbol{\nabla}\cdot\boldsymbol{u})\left(\left(\frac{\boldsymbol{v}^2}{2} + e - \frac{DP}{2\rho}\right)\left(\frac{\rho(\boldsymbol{v}-\boldsymbol{u})^2}{2P} - \frac{D}{2}\right) - \frac{DP}{2\rho}\right)f^{eq} \\ & + \left(\boldsymbol{\nabla}h - \frac{k}{\mu}\boldsymbol{\nabla}T\right)\cdot(\boldsymbol{v}-\boldsymbol{u})f^{eq}.\end{aligned} \tag{3.25}$$

The first term in (3.24) provides the Korteweg force contribution to the momentum balance, while its counterpart, the first term in (3.25), generates the corresponding work term in the bulk-energy balance (2.8). Furthermore, the second term in (3.24) and its counterpart in (3.25) define the bulk viscosity contributions to the momentum and bulk-energy-balance equations. Finally, the last term in (3.25) is the heat-flux correction required to recover Fourier's law, as discussed above.

(vii) The double-relaxation form of the kinetic (3.3), (3.4), (3.5) and (3.6) has the advantage of admitting the standard lattice Boltzmann space–time discretisation. Integration along characteristics combined with trapezoidal quadrature of the collision terms (He *et al.* 1998; Ansumali *et al.* 2007) yields an explicit, second-order accurate scheme (see details in Appendix B)

$$f(\boldsymbol{x}+\boldsymbol{v}\delta t, t+\delta t) = f + 2\beta\left(f^{eq} - f\right) + \frac{\delta t}{\lambda}(1-\beta)\left(f_\lambda^\star - f^{eq}\right), \tag{3.26}$$

$$g(\boldsymbol{x}+\boldsymbol{v}\delta t, t+\delta t) = g + 2\beta\left(g^{eq} - g\right) + \frac{\delta t}{\lambda}(1-\beta)\left(g_\lambda^\star - g^{eq}\right). \tag{3.27}$$

Here, all quantities on the right-hand side are evaluated at $(\boldsymbol{x}, t)$, δt is the time step and $\beta \in [0, 1]$, is the transformed relaxation parameter

$$\beta = \frac{\delta t}{2\tau + \delta t}. \tag{3.28}$$

As a consequence of the trapezoidal time integration, the transformed populations are related to the hydrodynamic fields ρ, $\boldsymbol{u}$ and E as follows:

$$\int mf\,\mathrm{d}\boldsymbol{v} = \rho, \tag{3.29}$$

$$\int m\boldsymbol{v}f\,\mathrm{d}\boldsymbol{v} = \rho\boldsymbol{u} - \frac{\delta t}{2}\boldsymbol{F}, \tag{3.30}$$

$$\int mg\,\mathrm{d}\boldsymbol{v} = \rho E - \frac{\delta t}{2}\boldsymbol{u}\cdot\boldsymbol{F}. \tag{3.31}$$

This concludes the presentation and analysis of the kinetic model for compressible non-ideal fluids. The lattice Boltzmann realisation follows.

3.2. *Lattice Boltzmann realisation*

In the lattice Boltzmann realisation of the kinetic model introduced above, we set $\lambda = \delta t$. We consider the standard $D3Q27$ discrete-velocity set $\boldsymbol{v}_i = c\boldsymbol{c}_i$ in $D = 3$ dimensions, with $Q = 27$ velocities

$$\boldsymbol{c}_i = (c_{ix}, c_{iy}, c_{iz}),\ \ c_{i\alpha} \in \{-1, 0, 1\}. \tag{3.32}$$

https://doi.org/10.1017/jfm.2026.11636 Published online by Cambridge University Press

The $D3Q27$ lattice (3.32) is characterised by the lattice speed of sound

$$\varsigma = \frac{1}{\sqrt{3}}c. \tag{3.33}$$

In the following, we use lattice units by setting $c = 1$. The discrete-velocity equations for the populations $f_i(\boldsymbol{x}, t)$ and $g_i(\boldsymbol{x}, t)$, $i = 1, \ldots, Q$, follow from (3.26) and (3.27) as

$$f_i(\boldsymbol{x} + \boldsymbol{v}_i\delta t, t + \delta t) = f_i + 2\beta\left(f_i^{eq} - f_i\right) + (1-\beta)\left(f_i^{\star} - f_i^{eq}\right), \tag{3.34}$$

$$g_i(\boldsymbol{x} + \boldsymbol{v}_i\delta t, t + \delta t) = g_i + 2\beta\left(g_i^{eq} - g_i\right) + (1-\beta)\left(g_i^{\star} - g_i^{eq}\right). \tag{3.35}$$

It remains, then, to define the equilibrium populations $\{f_i^{eq}, g_i^{eq}\}$ and the shifted-equilibrium populations $\{f_i^{\star}, g_i^{\star}\}$. To this end, we follow the product-form formalism (Karlin & Asinari 2010) and introduce functions in two variables, ξ_α and $\zeta_{\alpha\alpha}$

$$\Psi_{i\alpha}(\xi_\alpha, \zeta_{\alpha\alpha}) = 1 - c_{i\alpha}^2 + \frac{1}{2}\left[\left(3c_{i\alpha}^2 - 2\right)\zeta_{\alpha\alpha} + c_{i\alpha}\xi_\alpha\right],\ i = 1, \ldots, Q,\ \alpha = x, y, z. \tag{3.36}$$

The equilibrium populations f_i^{eq} are defined by setting the parameters in the functions (3.36) as follows:

$$\xi_\alpha^{eq} = u_\alpha, \tag{3.37}$$

$$\zeta_{\alpha\alpha}^{eq} = \theta + u_\alpha^2, \tag{3.38}$$

where θ is given by the thermodynamic flow work (3.18). With the definitions (3.37) and (3.38) in the functions (3.36), the local-equilibrium populations are written in product form

$$f_i^{eq} = \rho\prod_\alpha \Psi_{i\alpha}\left(u_\alpha, \theta + u_\alpha^2\right). \tag{3.39}$$

With $\lambda = \delta t$, the shifted flow velocity (3.11) and shifted reference temperature (3.12) are

$$\boldsymbol{u}^{\star} = \boldsymbol{u} + \delta t\left(\frac{\boldsymbol{F}}{\rho}\right), \tag{3.40}$$

$$\theta^{\star} = \theta + \delta t\alpha\theta\ (\boldsymbol{\nabla}\cdot\boldsymbol{u}). \tag{3.41}$$

For the shifted-equilibrium populations $f_i^{\star}$, the parameters ξ_α and $\zeta_{\alpha\alpha}$ in the functions (3.36) are set as follows:

$$\xi_\alpha^{\star} = u_\alpha^{\star}, \tag{3.42}$$

$$\zeta_{\alpha\alpha}^{\star} = \theta^{\star} + \left(u_\alpha^{\star}\right)^2 + \delta t\Phi_{\alpha\alpha}. \tag{3.43}$$

Compared with the continuous-velocity kinetic model of § 3.1, the discrete-velocity formulation requires the additional correction term

$$\Phi_{\alpha\alpha} = -\frac{1}{\rho}\partial_\alpha\left(\rho u_\alpha^3 + 3\rho u_\alpha(\theta - \varsigma^2)\right). \tag{3.44}$$

This is the standard correction necessary to restore Galilean invariance in the hydrodynamic limit on first-neighbour discrete-velocity lattices (Prasianakis & Karlin 2007; Li *et al.* 2012; Hosseini, Darabiha & Thévenin 2020). Combining (3.42) and (3.43) with the same product-form construction utilising (3.36), the shifted-equilibrium populations may be written as

$$f_i^{\star} = \rho\prod_\alpha \Psi_{i\alpha}\left(u_\alpha^{\star}, \theta^{\star} + \left(u_\alpha^{\star}\right)^2 + \delta t\Phi_{\alpha\alpha}\right), \tag{3.45}$$

https://doi.org/10.1017/jfm.2026.11636 Published online by Cambridge University Press

which completes the definition of the forcing term in (3.34).

For the g-populations, we follow the generating-function representation introduced in Karlin *et al.* (2013) and Saadat *et al.* (2021*b*). The generating function is the bulk energy per unit mass

$$E(\rho, \boldsymbol{u}, T) = e(\rho, T) + \frac{u^2}{2}, \tag{3.46}$$

consistent with (2.1). The corresponding equilibrium populations are constructed by repeated application of the operators

$$\mathcal{O}_\alpha(\theta) E = \theta \frac{\partial E}{\partial u_\alpha} + u_\alpha E, \tag{3.47}$$

whose dependence on the reference temperature is indicated explicitly. The discrete equilibrium g_i^{eq} is defined by setting $\xi_\alpha = \mathcal{O}_\alpha$ and $\zeta_{\alpha\alpha} = \mathcal{O}_\alpha^2$ in the functions (3.36) and interpreting the product-form as an operator acting on the generating function (3.46)

$$g_i^{eq}(\rho, \boldsymbol{u}, T, \theta) = \rho \prod_\alpha \Psi_{i\alpha} \left(\mathcal{O}_\alpha(\theta), [\mathcal{O}_\alpha(\theta)]^2 \right) E(\rho, \boldsymbol{u}, T). \tag{3.48}$$

Shifted-equilibrium populations $g_i^\star$ are defined using the equilibrium product-form (3.48) evaluated at shifted values (3.40) and (3.41), and adding a correction

$$g_i^\star = g_i^{eq}\left(\rho, \boldsymbol{u}^\star, T^\star, \theta^\star\right) + \begin{cases} \dfrac{1}{2} \boldsymbol{c}_i \cdot \boldsymbol{q}^c, & c_i^2 = 1, \\ 0, & \text{otherwise}, \end{cases} \tag{3.49}$$

where the non-equilibrium energy flux $\boldsymbol{q}^c$ and shifted temperature $T^\star$ are given by (3.16) and (3.13), respectively, with $\lambda = \delta t$

$$T^\star = T - \delta t^2 \left(\frac{\boldsymbol{F} \cdot \boldsymbol{F}}{2\rho^2 c_v} \right), \tag{3.50}$$

$$\boldsymbol{q}^c = \delta t P \left(\nabla h - \frac{k}{\mu} \nabla T \right). \tag{3.51}$$

Finally, the locally conserved fields entering the equilibrium and shifted-equilibrium populations, namely the density ρ, the momentum $\rho \boldsymbol{u}$ and the bulk energy ρE, are defined from the zeroth- and first-order moments of the populations, as in (3.29), (3.30) and (3.31), with sums over discrete velocities replacing velocity-space integrals

$$\rho = \sum_{i=1}^{Q} f_i, \tag{3.52}$$

$$\rho \boldsymbol{u} = \sum_{i=1}^{Q} \boldsymbol{c}_i f_i + \frac{\delta t}{2} \boldsymbol{F}, \tag{3.53}$$

$$\rho E = \sum_{i=1}^{Q} g_i + \frac{\delta t}{2} \boldsymbol{u} \cdot \boldsymbol{F}. \tag{3.54}$$

Once the bulk energy E is computed from (3.54), the thermodynamic temperature follows from the caloric equation obtained by integrating (2.5). For a van der Waals fluid, as the equation of state (2.31) is linear in T, c_v exhibits no density dependence. Integrating (2.5)

https://doi.org/10.1017/jfm.2026.11636 Published online by Cambridge University Press

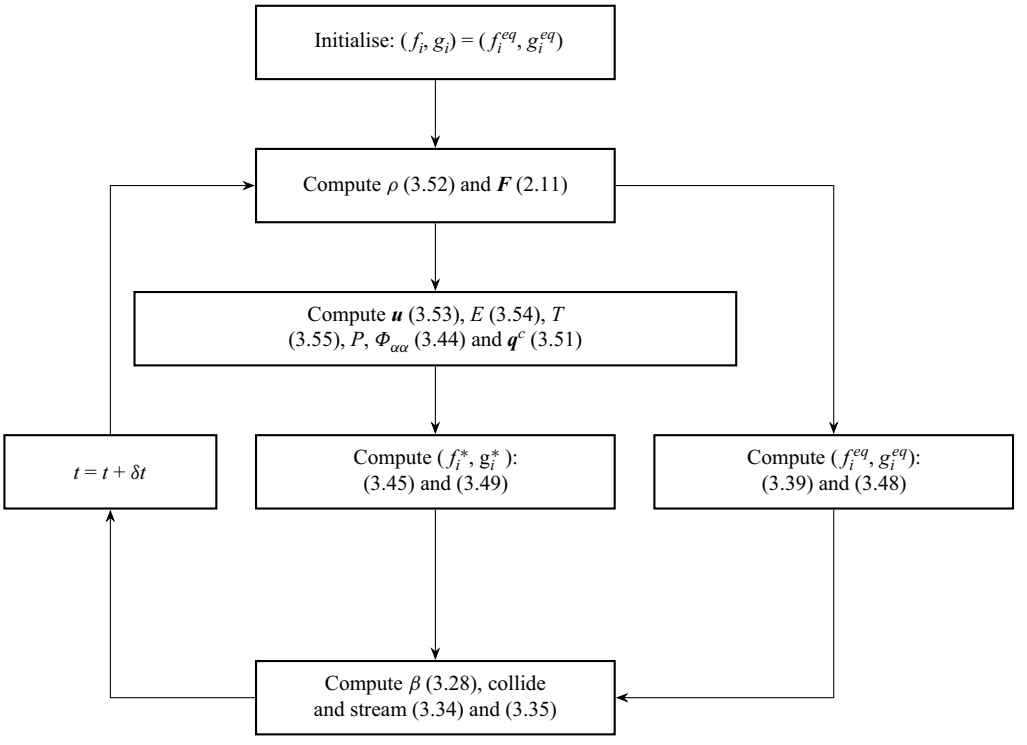


Figure 2. Overall structure of the proposed algorithm for the simulation of compressible non-ideal flows.

therefore gives the explicit relation

$$T = \frac{E - \boldsymbol{u}^2/2 + a\rho}{c_v}. \tag{3.55}$$

This explicit inversion is specific to equations of state with this simple caloric structure. For more general equations of state, such as the Peng–Robinson equation, the temperature must instead be recovered at each node by solving the corresponding nonlinear caloric relation.

Evaluating $\boldsymbol{F}$, $\Phi_{\alpha\alpha}$ and $\boldsymbol{q}^c$ requires spatial derivatives of ρ, T, h and $\boldsymbol{u}$. In the numerical applications below, all derivatives are computed using standard central second-order accurate finite differences, except for the first-order derivative in (3.44). This term is evaluated using an upwind-biased approximation, for instance along the x-axis

$$\Phi_{xx} = \frac{1 + \mathrm{sgn}(u_x)}{2} \frac{\Lambda_x|_x - \Lambda_x|_{x-\delta x}}{\delta x} + \frac{1 - \mathrm{sgn}(u_x)}{2} \frac{\Lambda_x|_{x+\delta x} - \Lambda_x|_x}{\delta x}, \tag{3.56}$$

where $\mathrm{sgn}(u_x)$ is the sign of u_x and

$$\Lambda_x = \rho u_x^3 + 3\rho u_x(\theta - \varsigma^2). \tag{3.57}$$

This upwind-biased approximation, while maintaining the formal order of accuracy of the solver, has been shown to improve stability in higher Mach number simulations (Hosseini *et al.* 2020; Renard *et al.* 2021; Saadat *et al.* 2021*a*).

The overall structure of the proposed algorithm is shown in figure 2. A detailed multi-scale analysis of the hydrodynamic limit is presented in Appendix C, demonstrating that

https://doi.org/10.1017/jfm.2026.11636 Published online by Cambridge University Press

Substance	R/c_v	P_c [Pa]	ρ_c [kg m^{-3}]	T_c [K]
Nitrogen	0.4	3.4×10^6	241.96	126.2

Table 1. Critical properties of nitrogen N_2. The critical density used here comes from fitting critical temperature and pressure from Jacobsen, Stewart & Jahangiri (1986) to the van der Waals equation of state.

the present lattice Boltzmann model recovers the hydrodynamic set (2.6), (2.7) and (2.8). Numerical applications and validation of the model are presented in the next section.

4. Numerical applications

4.1. *Consistency: dispersion and dissipation of hydrodynamic modes*

As a first step, we probe the dispersion and dissipation properties of the hydrodynamic shear, normal and entropic modes in the limit of a resolved flow. These benchmarks will consider: (a) speed of sound, (b) shear wave dissipation, (c) shear stress, viscous heating and entropic-mode dissipation and (d) the normal-mode dissipation rate. In all cases, and without loss of generality, we consider a van der Waals fluid fitted to the critical properties of nitrogen N_2, which are listed in table 1. Below, the subscript r refers to reduced variables normalised by their value at the critical point.

The set-up for investigating the speed of sound consists of a one-dimensional domain of size $L_x = 0.1$ m discretised with the spacing $\delta x = 10\,\mu$m. The initial conditions are

$$P(x) = \begin{cases} P_0, & x \leqslant L_x/2, \\ P_0 + \delta P, & x > L_x/2, \end{cases}, \tag{4.1}$$

$$u_x(x) = u_{x0}, \tag{4.2}$$

$$T(x) = T_0. \tag{4.3}$$

Once the initial conditions are set, the system is left to evolve, resulting in two oppositely moving pressure fronts propagating at a speed that becomes constant after a short initial transition time. For sufficiently weak perturbations, this corresponds to the speed of sound in the system. A series of such cases with different initial conditions were run on both liquid and vapour branches of the saturation curve for $T_0 \in [88.34, 126.2]$ K corresponding to $T_0/T_c \in [0.7, 1]$ and compared with the analytical speed of sound (2.17) for the van der Waals equation of state (2.31)

$$c_s = \sqrt{\frac{RT(1 + R/c_v)}{(1 - b\rho)^2} - 2a\rho}. \tag{4.4}$$

Note that for a saturated vapour/liquid, fixing T_0 sets ρ_0 and P_0 via Maxwell's equal-area construction and the equation of state. The results are shown in figure 3 and are in excellent agreement.

The next test is a measurement of the effective shear viscosity. For this, we set up a pseudo-one-dimensional, periodic domain of size $L_x = 0.1$ m, discretised with $N_x \times N_y = 100 \times 1$ grid points. The initial conditions are set as follows:

$$u_y(x) = Ma_y c_s(\rho_0, T_0) + \delta Ma_y c_s(\rho_0, T_0) \sin\left(\frac{2\pi x}{L_x}\right), \tag{4.5}$$

$$u_x(x) = 0, \tag{4.6}$$

$$\rho(x) = \rho_0, \tag{4.7}$$

https://doi.org/10.1017/jfm.2026.11636 Published online by Cambridge University Press

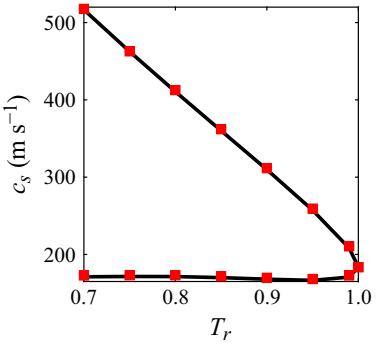


Figure 3. Speed of sound for nitrogen N_2 on the saturated liquid and vapour branches. Line: analytical solution from (4.4); markers: simulations.

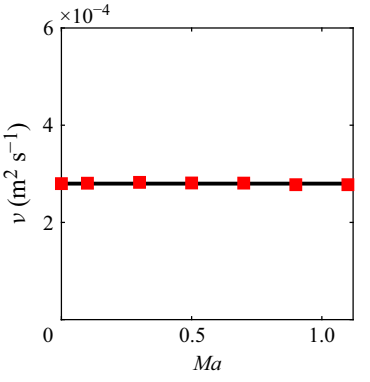


Figure 4. Kinematic viscosity as measured from shear wave decay simulations at different Mach numbers. Solid black line: analytical viscosity; square markers: viscosity measured from simulations.

$$T(x) = T_0. \tag{4.8}$$

The maximum amplitude of the perturbation, $u_y - Ma_y c_s(\rho_0, T_0)$, in the domain is monitored throughout the simulation, and its evolution over time is fitted with an exponential decay function

$$u_y^{max}(t) \propto \exp\left(-\frac{4\pi^2}{L_x^2}\frac{\mu}{\rho}t\right). \tag{4.9}$$

The viscosity measured from simulations is compared with that predicted from the multi-scale analysis. The results, shown in figure 4, demonstrate excellent agreement and Galilean invariance of the measured viscosity.

Next, we probe the thermal conductivity by monitoring the dissipation rate of temperature perturbations. The configuration consists of a pseudo-one-dimensional, periodic domain of size $L_x \times L_y = 0.1\ \text{m} \times 0.001\ \text{m}$. Initial conditions are set as follows:

$$\rho(x) = \rho_0 + \delta\rho \sin\left(\frac{2\pi x}{L_x}\right), \tag{4.10}$$

$$P(x) = P_0(\rho_0, T_0), \tag{4.11}$$

$$T(x) = T(\rho(x), P_0), \tag{4.12}$$

$$u_x(x) = Ma_x c_s(\rho_0, T_0), \tag{4.13}$$

https://doi.org/10.1017/jfm.2026.11636 Published online by Cambridge University Press

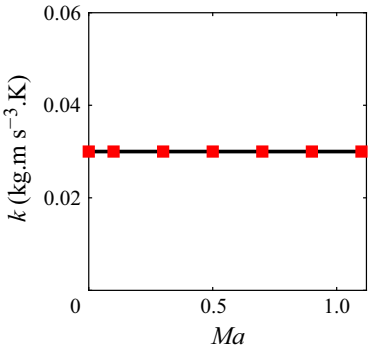


Figure 5. Thermal conductivity as measured from simulations at different Mach numbers. Plain black line: analytical thermal conductivity; square markers: thermal conductivity measured from simulations.

$$u_y(x) = 0, \tag{4.14}$$

where $T(\rho(x),\, P_0)$ is obtained from the equation of state. We then monitor the maximum of the temperature in the domain T^{max} and extract the thermal conductivity by fitting the data to

$$|T^{max} - T_0| \propto \exp\left(-\frac{4\pi^2}{L_x^2}\frac{k}{\rho_0 c_p(\rho_0,\, T_0)}t\right). \tag{4.15}$$

The measured thermal conductivities are then compared with the imposed value. Results are shown in figure 5 and are found to be in excellent agreement with the imposed value.

To validate both viscous heating and the dissipation rate of the entropic modes, we next consider the two-dimensional thermal Couette flow. The case consists of a pseudo-one-dimensional domain of size L_x with walls at $x = 0$ and $x = L_x$ and periodic boundary conditions along the y-direction. The flow is subject to the following boundary conditions:

$$\{u_x,\, u_y,\, T\}(x = 0) = \{0,\, 0,\, T_w\}, \tag{4.16}$$

$$\{u_x,\, u_y,\, T\}(x = L_x) = \{0,\, U_w,\, T_w\}. \tag{4.17}$$

The analytical steady-state solution to this configuration can readily be derived as

$$u_y(x) = U_w\frac{x}{L_x}, \tag{4.18}$$

$$T(x) = T_w + \frac{\mu U_w^2}{2k}\frac{x}{L_x}\left(1 - \frac{x}{L_x}\right). \tag{4.19}$$

To validate the model, we consider a domain of size $L_x = 1$ mm discretised with 100 grid points. Simulations were performed for $Pr \in \{0.6,\, 1.2,\, 4.9\}$ and $Ma \in \{0.8,\, 1.2,\, 1.6\}$. The results are displayed in figure 6 and show excellent agreement with the analytical solutions.

Finally, we examine the dissipation rate of normal modes, i.e. acoustics. To do this, we set up a pseudo-one-dimensional domain of size L_x with periodic boundary conditions in both the x- and y-directions. Defining a uniform background state, $(\rho_0,\, T_0,\, P_0)$, we add a small perturbation to it at $t = 0$

$$u_x(x) = Ma_x c_s(\rho_0,\, T_0), \tag{4.20}$$

$$u_y(x) = 0, \tag{4.21}$$

$$P(x) = P_0 + \delta P \sin\left(\frac{2\pi x}{L_x}\right). \tag{4.22}$$

https://doi.org/10.1017/jfm.2026.11636 Published online by Cambridge University Press

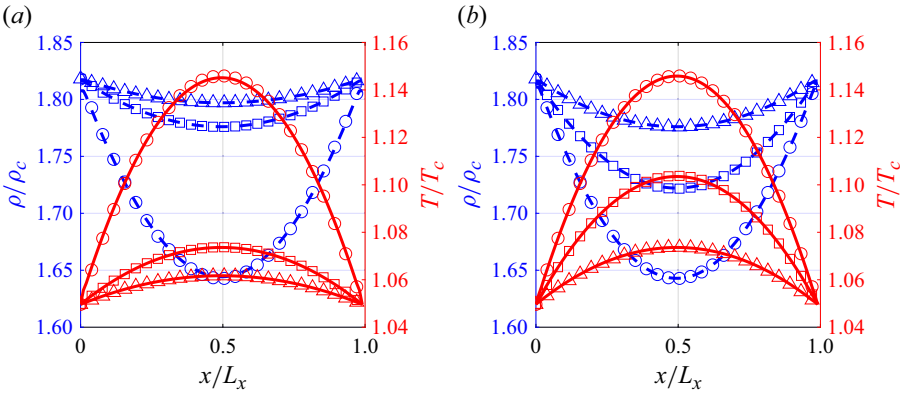


Figure 6. Left panel: temperature and density distribution across the channel for the thermal Couette flow at different Prandtl numbers. Triangle, square and circular markers are analytical results for $Pr \in \{0.6, 1.2, 4.9\}$ respectively. Solid and dashed lines are temperature and density profiles from simulations. Here, $Ma = 0.8$ for all cases. Right panel: temperature and density distribution for different Mach numbers. Triangle, square and circular markers are analytical results for $Ma \in \{0.8, 1.2, 1.6\}$ respectively. Solid and dashed lines are temperature and density profiles from simulations. Here, $Pr = 1.2$ for all cases.

The density and temperature fields can be computed using isentropic relations for the van der Waals fluid (Kouremenos, Antonopoulos & Kakatsios 1988; Nederstigt & Pecnik 2023)

$$\frac{P_0}{\rho_0^{\gamma^0_{P\rho}}} = \frac{P}{\rho^{\gamma_{P\rho}}}, \tag{4.23}$$

$$\frac{T_0}{\rho_0^{\gamma^0_{T\rho}-1}} = \frac{T}{\rho^{\gamma_{T\rho}-1}}, \tag{4.24}$$

where

$$\gamma_{P\rho} = \frac{\rho}{P}\frac{c_p}{c_v}\left(\frac{\partial P}{\partial \rho}\right)_T, \tag{4.25}$$

$$\gamma_{T\rho} = \frac{1}{\rho c_v}\left(\frac{\partial P}{\partial T}\right)_\rho + 1. \tag{4.26}$$

Here c_p is the specific heat at constant pressure

$$c_p = c_v + T\left(\frac{\partial P}{\partial T}\right)_v \left(\frac{\partial v}{\partial T}\right)_P, \tag{4.27}$$

which for the van der Waals equation of state leads to

$$c_p = c_v + \frac{R^2 T}{RT - 2a\rho(1-b\rho)^2}. \tag{4.28}$$

In the ideal-gas limit $P \to \rho RT$, both exponents reduce to $(\gamma_{P\rho}, \gamma_{T\rho}) \to c_p/c_v$. We leave the system to evolve over time and monitor the acoustic energy (Landau & Lifshitz 1987)

$$E_{acoustic} = \frac{1}{2}\int \left[\rho_0 |\boldsymbol{u} - \boldsymbol{u}_0|^2 + \frac{\rho'^2 c_s^2(\rho_0, P_0)}{\rho_0}\right] \mathrm{d}x, \tag{4.29}$$

https://doi.org/10.1017/jfm.2026.11636 Published online by Cambridge University Press

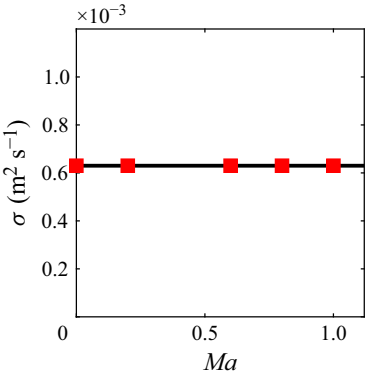


Figure 7. Normal dissipation rate σ as measured from normal wave decay simulations at different Mach numbers. Plain black line: analytical dissipation rate, square markers: dissipation rate measured from simulations.

where $\rho' = \rho - \rho_0$. It can readily be shown that the decay for a propagating plane wave is proportional to

$$E_{acoustic} \propto \exp\left(-\frac{4\pi^2}{L_x^2}\sigma t\right), \tag{4.30}$$

where (Landau & Lifshitz 1987)

$$\sigma = \frac{2(D-1)}{D}\frac{\mu}{\rho} + \frac{\eta}{\rho} + \frac{k}{\rho c_p}\left(\frac{c_p}{c_v} - 1\right). \tag{4.31}$$

Simulations were conducted for different initial velocities and effective dissipation rates measured. Results are shown in figure 7. The results show very good agreement with the analytical predictions.

4.2. *Multi-phase regime*

4.2.1. *Liquid–vapour co-existence*

Turning to the two-phase regime, we first probe the liquid–vapour co-existence densities as a validation of thermodynamic and mechanical consistency. Simulations are conducted in a pseudo-one-dimensional domain of size $L_x = 0.4$ mm with periodic boundary conditions. The domain is filled with saturated vapour, with a column of saturated liquid in the centre. Simulations are evolved until the density field converges. Simulations were run for $T_r \in [0.3, 0.99]$. As shown in figure 8, numerical results agree closely with the reference values obtained using Maxwell's equal-area construction.

4.2.2. *Interface consistency and convergence*

To illustrate the consistency of the proposed solver, we repeat the nitrogen liquid–vapour co-existence density test described above, assessing the convergence of the interface with increasing resolution. All physical parameters are unchanged: the nitrogen properties are those listed in table 1, the reduced temperature is $T_r = 0.9$ with corresponding co-existence densities $(\rho^l, \rho^v) = (399.8, 102.71)$ kg m^{-3}, and the capillarity coefficient is set to $\kappa = 10^{-10}$ m^7 kg^{-1} s^{-2}. The computational domain has a length of $L_x = 0.5$ mm. Simulations are conducted at the various resolutions detailed in table 2. The results obtained from simulations are compared with data from a high-resolution iterative finite-difference solver for

$$\partial_x P = \kappa\rho\partial_x^3\rho, \tag{4.32}$$

https://doi.org/10.1017/jfm.2026.11636 Published online by Cambridge University Press

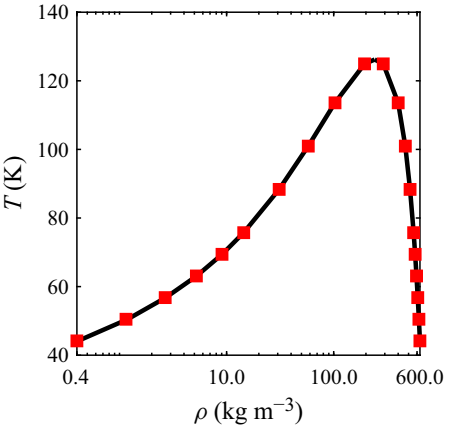


Figure 8. Liquid–vapour co-existence densities for nitrogen N_2. Line: Maxwell's equal-area rule; symbols: simulation.

Case	δx	δt
1	0.1 μm	2.5×10^{-11} s
2	0.5 μm	1.25×10^{-10} s
3	1 μm	2.5×10^{-10} s
4	5 μm	1.25×10^{-9} s

Table 2. Grid properties for the nitrogen N_2 liquid–vapour interface simulations.

and are shown in figure 9. The results demonstrate both excellent agreement with the reference solution and convergence under grid refinement. To further quantify solver convergence, we compare the simulated vapour density with the reference value obtained from Maxwell's equal-area construction. The results, shown in figure 10, exhibit second-order convergence.

4.3. *Compressible configurations*

4.3.1. *One-dimensional non-ideal shock tubes*

Until the early 1980s, shock-tube experiments were limited to gases exhibiting classical wave behaviour. Borisov *et al.* (1983) first reported a shock-tube experiment aimed at investigating non-classical wave phenomena in a dense gas, i.e. near the thermodynamic critical point. The nonlinear dynamics of gases is characterised, to a large extent, by the fundamental derivative of gas dynamics (Thompson 1971)

$$\Gamma = 1 + \frac{\rho}{c_s}\left(\frac{\partial c_s}{\partial \rho}\right)_s . \tag{4.33}$$

For simple waves, Γ represents the rate of change of the convected sound speed with respect to density. When $\Gamma > 0$, the flow exhibits positive nonlinearity, i.e. disturbances steepen forward to form compression shocks. In contrast, when $\Gamma < 0$, negative nonlinearity occurs and disturbances steepen backward, leading to expansion shocks. In regions of negative nonlinearity, gases display distinct non-classical phenomena.

Following Argrow (1996), we illustrate non-classical wave fields using three non-ideal shock-tube cases, each with flow regions wholly or partly in the regime of negative

https://doi.org/10.1017/jfm.2026.11636 Published online by Cambridge University Press

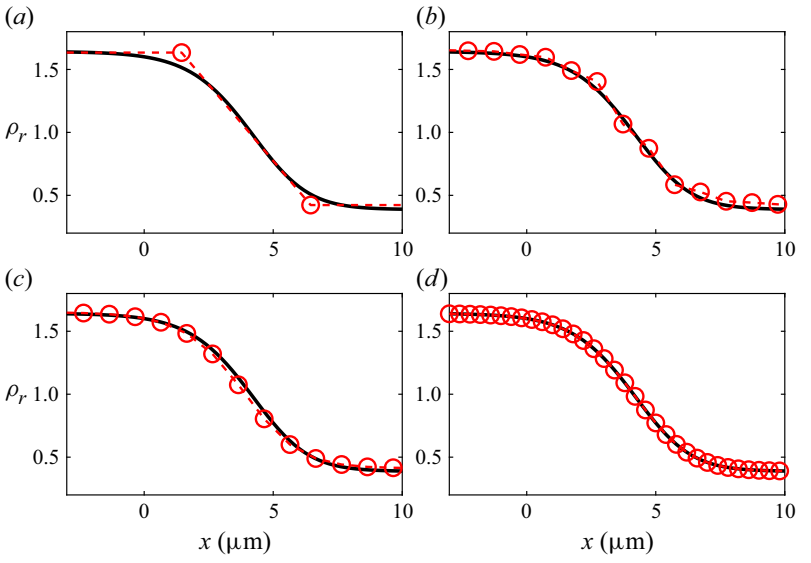


Figure 9. Liquid–vapour interface for nitrogen N_2 at $T_r = 0.9$. Black lines are converged results from implicit finite-difference solver and red markers from LBM simulations. Top left panel: $\delta x = 5\,\mu$m and top right panel: $\delta x = 1\,\mu$m. Bottom left panel: $\delta x = 0.5\,\mu$m. Bottom right panel: $\delta x = 0.1\,\mu$m.

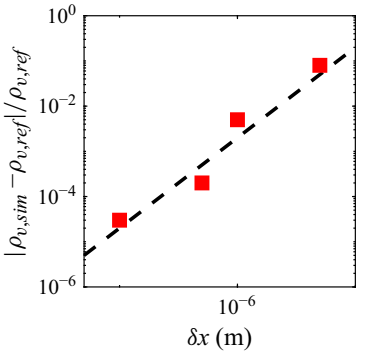


Figure 10. Convergence of the vapour-phase density for nitrogen N_2 at $T_r = 0.9$. Markers are results from simulations while the dashed line indicates second-order convergence.

nonlinearity. In all three cases, simulations consist of a one-dimensional domain of size $L_x = 1$m, initially divided into left and right halves. The initial conditions set for each half are listed in table 3. In all cases, the grid size is set to $\delta x = 0.001$ m. Other simulation-specific parameters are listed in table 4. Note that the Courant–Friedrichs–Lewy (CFL) is here defined as the convective CFL

$$\mathrm{CFL} = \frac{\|\boldsymbol{u}\|}{\delta x/\delta t}, \tag{4.34}$$

where $\|\boldsymbol{u}\| = \sqrt{\boldsymbol{u}\cdot\boldsymbol{u}}$. In all cases, the initial discontinuity is located at half the length of the domain. The results for case I are shown and compared with the reference data in figure 11. This configuration is a typical example of non-classical gas dynamics: first, a compression front is observed moving from the high-pressure region to low-pressure region of the domain. In classical gas dynamics, one expects a sharp compression front, which is not

https://doi.org/10.1017/jfm.2026.11636 Published online by Cambridge University Press

Case	R/c_v	$(P_r, \rho_r)_{left}$	$(P_r, \rho_r)_{right}$
I	0.0125	(1.09,0.879)	(0.885,0.562)
II	0.329	(1.6077,1.01)	(0.8957,0.594)
III	0.0125	(3.00,1.818)	(0.575,0.275)

Table 3. List of initial conditions for shock-tube cases.

Case	δx	δt	Maximum CFL	Maximum Ma
I	0.001 m	8.3 μs	0.4998	0.45
II	0.001 m	4 μs	0.4226	0.196
III	0.001 m	2.86 μs	0.4538	1.846

Table 4. Numerical parameters for the shock-tube cases.

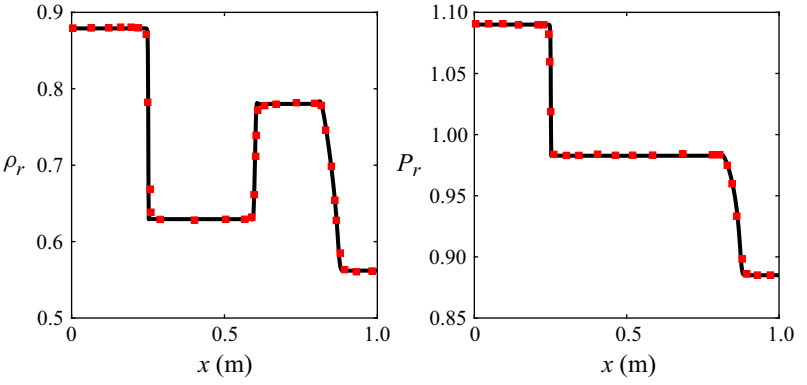


Figure 11. Reduced density and pressure fields for shock tube I at time $t = 0.45 L_x \sqrt{\rho_c / P_c}$. Solid lines are reference data from Guardone & Vigevano (2002) and markers denote simulation results.

observed here. A second front, moving in the opposing direction, from the low-pressure region to the high-pressure region, known as a rarefaction front, is also observed. Contrary to classical gas-dynamic expectations, this front is sharp. Such non-classical wave fronts have recently been observed experimentally by Colonna *et al.* (2026).

These observations can be explained by looking into the fundamental derivative of gas dynamics (4.33), which, in the case of a van der Waals fluid, can be computed explicitly as

$$\Gamma(P, \rho) = \frac{(R/c_v + 1)\,(R/c_v + 2)\,\dfrac{P + a\rho^2}{(1/\rho - b)^2} - 6a\rho^4}{2\,(R/c_v + 1)\,\dfrac{P + a\rho^2}{(1/\rho - b)} - 4a\rho^4}. \tag{4.35}$$

It is observed in figure 12 that all points in the domain at $t = 0.45 L_x \sqrt{\rho_c / P_c}$ fall within the $\Gamma < 0$ region. Physically, Γ measures how the sound speed changes with compression or expansion along an isentrope. It directly controls the nonlinearity of acoustic waves. Consider first the compression front; along the front, both pressure and density decrease.

https://doi.org/10.1017/jfm.2026.11636 Published online by Cambridge University Press

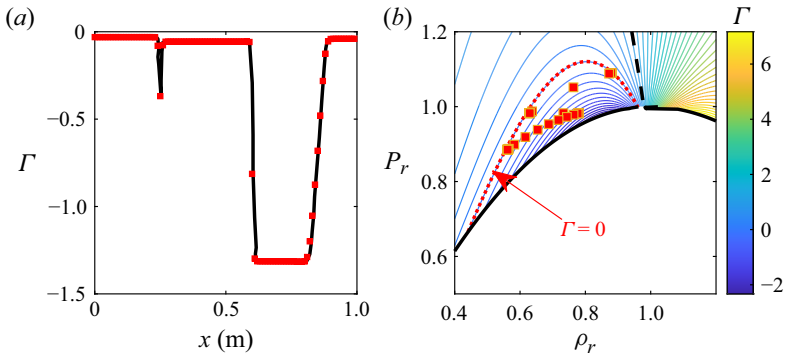


Figure 12. (*a*) Fundamental derivative Γ distribution for shock tube I at $t = 0.45L_x\sqrt{\rho_c/P_c}$. Solid lines are reference data from Guardone & Vigevano (2002) and markers are from simulations. (*b*) Fundamental derivative Γ iso-contours in P_r–ρ_r plane. Red square symbols represent the state of the shock tube shown on the left panel. The solid black line is the co-existence curve. Dashed black line represents $\Gamma = 1$.

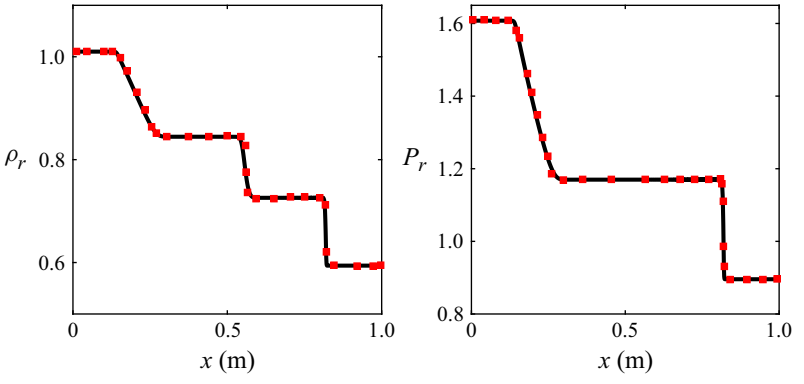


Figure 13. Reduced density and pressure fields for shock tube II at time $t = 0.2L_x\sqrt{\rho_c/P_c}$. Solid lines are reference data from Guardone & Vigevano (2002) and markers are from simulations.

When the $\Gamma < 0$, the characteristic speeds decrease with increasing pressure (or density). Consequently, the local propagation speed is smaller in the higher-pressure region behind the front than in the lower-pressure region ahead of it. As a result, characteristics diverge across the compression region, causing the initially sharp front to spread. The compression wave therefore evolves into a compression fan rather than steepening into a discontinuity. Next consider the rarefaction wave; along this direction, pressure and density also decrease. For $\Gamma < 0$, the characteristic speeds increase as pressure (or density) decreases. This leads to a convergence of characteristics, causing the rarefaction wave to steepen and the front to sharpen. In figure 11 one can clearly observe a rarefaction shock moving from right to left, i.e. low to high pressure. Additionally, one also observes a compression fan propagating into the low-pressure region.

In the second configuration, the fronts appear to follow the classical gas-dynamic behaviour. As shown in figure 13, in agreement with reference data, both pressure and density fields show a compression front moving towards the low-pressure side and a rarefaction wave moving in the opposite direction. To further confirm the classical characteristics of this shock-tube case, we plot the distribution of Γ at $t = 0.2L_x\sqrt{\rho_c/P_c}$ in figure 14.

https://doi.org/10.1017/jfm.2026.11636 Published online by Cambridge University Press

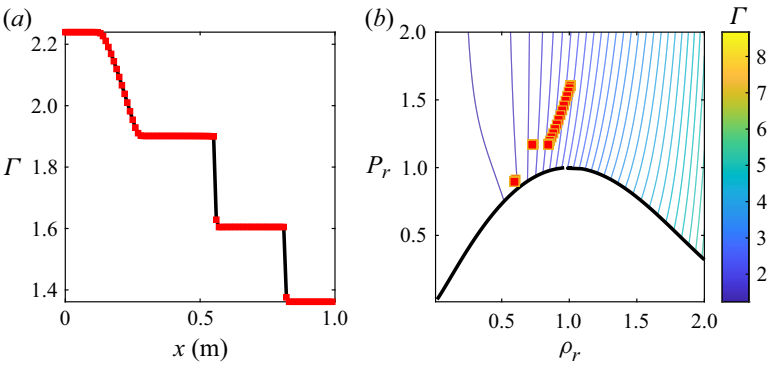


Figure 14. (*a*) Fundamental derivative Γ distribution for shock tube II at $t = 0.2L_x\sqrt{\rho_c/P_c}$. Solid lines are reference data from Guardone & Vigevano (2002) and markers are from simulations. (*b*) Fundamental derivative Γ iso-contours in P_r–ρ_r plane. red square symbols represent the state of the shock tube shown on the left in the P_r–ρ_r space. The solid black line is the co-existence curve.

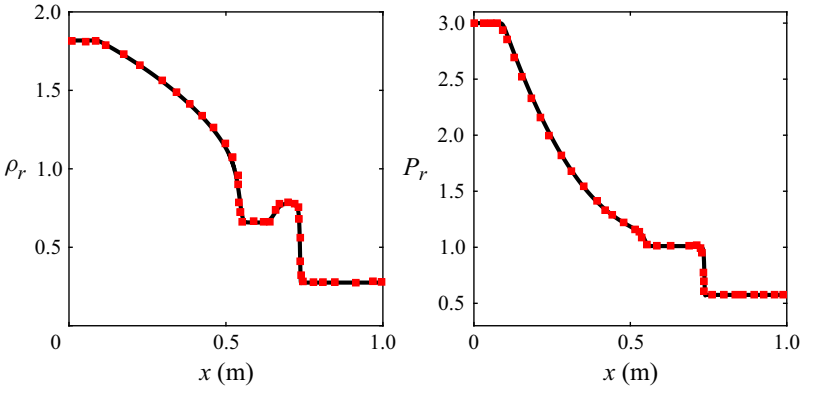


Figure 15. Reduced density and pressure fields for shock tube III at time $t = 0.15L_x\sqrt{\rho_c/P_c}$. Solid lines are reference data from Guardone & Vigevano (2002) and markers are from simulations.

In agreement with the reference data, Γ remains positive throughout the domain. As in the previous shock-tube configuration, the thermodynamic states sampled by the flow lie in the supercritical region and close to the saturation line. However, because of the considerably lower specific heat capacity compared with case I, no negative-Γ region is encountered in the present case. This indicates that non-classical BZT effects are strongly influenced by the specific heat capacity and are therefore more likely to arise in fluids composed of larger, more complex molecules with higher specific heat capacities.

Finally, in the third shock-tube experiment both initial states remain in the classical region. Figure 15 shows the density and pressure profiles for this shock tube at $t = 0.15L_x\sqrt{\rho_c/P_c}$. As in the previous configurations, a rarefaction front propagates leftward towards the dense region. Its structure, however, is non-classical: the front initially resembles a rarefaction fan, but sharpens near $x = 0.5$ m. This behaviour can be explained using the fundamental derivative shown in figure 16. For $x \lesssim 0.5$ m, $\Gamma > 1$ and the expansion behaves classically. Near $x = 0.5$ m, Γ becomes negative; consequently the rarefaction wave steepens into a shock. A second sign change of Γ occurs on the compression side, where the flow crosses back from the non-classical regime, associated

https://doi.org/10.1017/jfm.2026.11636 Published online by Cambridge University Press

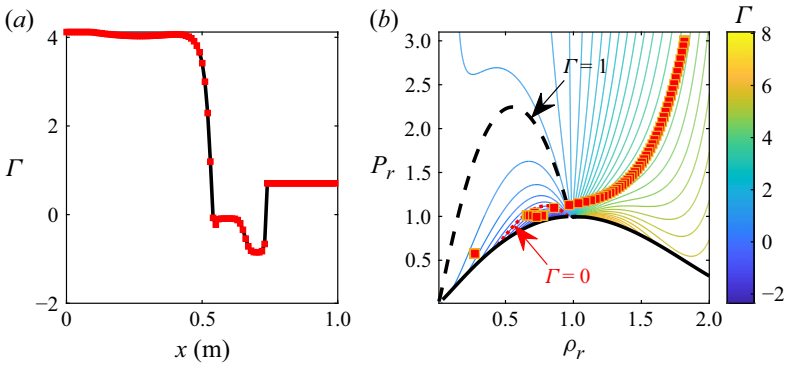


Figure 16. (*a*) Fundamental derivative Γ distribution for shock tube III at $t = 0.15 L_x \sqrt{\rho_c / P_c}$. Solid lines are reference data from Guardone & Vigevano (2002) and markers are from simulations. (*b*) Fundamental derivative Γ iso-contours in P_r–ρ_r plane. Red square symbols represent the state of the shock tube shown in the left in the P_r–ρ_r space. The solid black line is the co-existence curve.

with a compression fan, into the classical regime, where the compression front steepens into a shock.

All three configurations show excellent agreement with reference data and demonstrate that the model properly captures the behaviour of a non-classical compressible gas.

4.4. *Shock–liquid-column interaction*

In our final application, we showcase the suitability of the model for compressible regimes, by considering the case of a circular liquid column interacting with a planar shock wave. The case consists of a two-dimensional domain of size $L_x \times L_y$, here resolved with 800 × 800 grid points, divided into subdomains via a shock positioned at x_s. On the right-hand side of the shock front, the pre-shock state $(\rho_1, T_1, u_{x,1})$ is set to that of a saturated vapour at $T_r = 0.9$, following Reyhanian *et al.* (2020). The post-shock state to the left of the shock front, $(\rho_2, T_2, u_{x,2})$, is derived using the Rankine–Hugoniot conditions. Furthermore, a saturated liquid column of radius R at $T_r = 0.9$, resolved with 65 grid points, is placed at (x_c, y_c) in the pre-shock domain. Times are non-dimensionalised by the characteristic scale $t_0 = (2R_0 c_s^v / u_s c_s^l)\sqrt{\rho^l / \rho^v}$ where u_s is the shock speed, $\rho^{l,v}$ are the liquid–vapour densities and $c_s^{l,v}$ are the saturated liquid–vapour speeds of sound. The shock speed is defined via the shock Mach number Ma_s as $u_s = Ma_s c_s^v$.

To further stabilise simulations, especially near sharp fronts, we use a nonlinear numerical-viscosity scheme as devised in Cook & Cabot (2004) and Fiorina & Lele (2005). This amounts to adding a numerical contribution to the transport coefficients as follows:

$$\{\mu, \eta, k\}^{eff} = \{\mu, \eta, k\} + \{\mu, \eta, k\}^{num}. \tag{4.36}$$

The numerical contributions are defined as

$$\{\mu, \eta\}^{num} = \rho C_{\{\mu,\eta\}} \delta x^{r+1} \overline{|\nabla^{r-1} S|}, \tag{4.37}$$

where

$$S = \frac{1}{2}\sqrt{\left(\nabla \boldsymbol{u} + \nabla \boldsymbol{u}^{\dagger}\right) : \left(\nabla \boldsymbol{u} + \nabla \boldsymbol{u}^{\dagger}\right)}, \tag{4.38}$$

https://doi.org/10.1017/jfm.2026.11636 Published online by Cambridge University Press

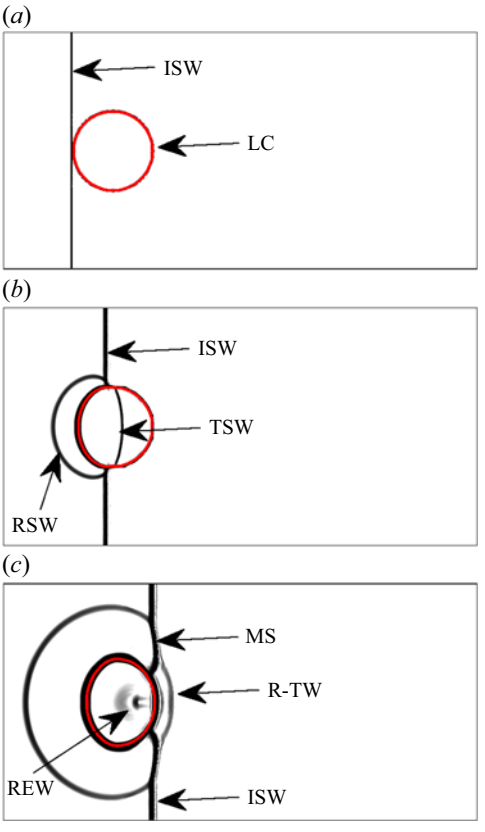


Figure 17. Schlieren images of shock–liquid-column interaction case at, from top to bottom, $t/t_0 = 0$, $t/t_0 = 0.3$ and $t/t_0 = 0.7$. Schlieren images are generated as $\phi = \exp(-a(\|\nabla\rho\|/\max(\|\nabla\rho\|)))$ with $a = 100$. The visualisation follows Quirk & Karni (1996) and Meng & Colonius (2015). Solid red lines indicate the liquid-column interface identified from a density level; ISW: incident shock wave; LC: liquid column; TSW: transmitted shock wave; RSW: reflected shock wave; MS: Mach stem; R-TW: retransmitted wave; REW: reflected expansion wave.

and the overbar in (4.37) indicates a Gaussian filter. Furthermore (Fiorina & Lele 2005)

$$k^{num} = \rho c_s C_k \delta x^{r+1} \overline{|\nabla^{r-1}|\nabla s||}, \tag{4.39}$$

with the entropy gradient obtained from (2.33) as

$$\nabla s = \frac{c_v}{T}\nabla T - \frac{R}{\rho(1-b\rho)}\nabla\rho. \tag{4.40}$$

Here, to minimise the numerical dissipation we have set $r = 5$. The flow evolution, represented by a Schlieren image for $Ma_s = 1.47$ is shown in figure 17. The wave structures that arise during the initial stages of the shock–liquid-column interaction are commonly used to validate numerical schemes. In the present study, representative wave patterns are extracted and illustrated in figure 17. Only the early-stage interaction between a planar shock wave and a cylindrical liquid column is considered here. As the incident shock wave travels from left to right across the liquid column, both a transmitted wave and a reflected shock wave are generated. The reflected shock wave propagates upstream into the surrounding vapour, while the transmitted wave moves downstream within the liquid column. Notably, the transmitted shock wave moves faster than the incident shock

https://doi.org/10.1017/jfm.2026.11636 Published online by Cambridge University Press

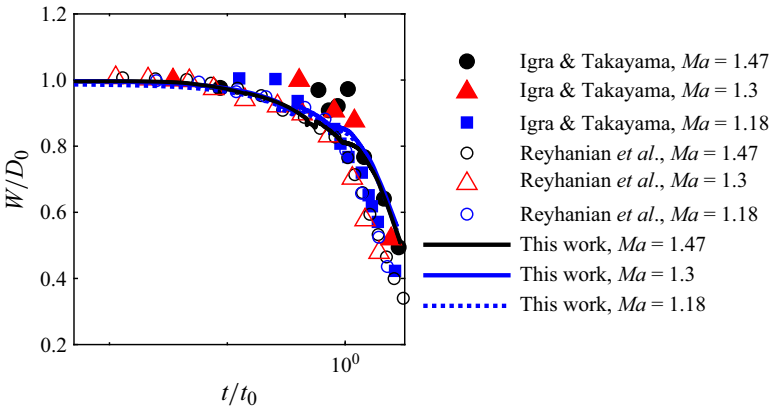


Figure 18. Evolution of the column width W along x-axis over time for three different Mach numbers. Simulations: (solid black line) $Ma_s = 1.47$, (red dashed line) $Ma = 1.3$ and (blue dotted line) $Ma_s = 1.18$. Experiments (Igra & Takayama 2001): (black filled circular markers) $Ma = 1.47$, (red filled triangle markers) $Ma = 1.3$ and (blue filled square markers) $Ma = 1.18$. Numerical results from Reyhanian *et al.* (2020): (black unfilled circular markers) $Ma = 1.47$, (red unfilled triangle markers) $Ma = 1.3$ and (blue unfilled square markers) $Ma = 1.18$.

wave, as the speed of sound in the liquid is larger than that in the vapour phase. Upon reaching the downstream interface of the column, the transmitted wave re-emerges into the downstream vapour. Simultaneously, expansion waves reflect repeatedly within the liquid column. At the upper lateral edge of the liquid column, the incident shock wave, the Mach stem and the slip line intersect to form a triple point. These wave structures along with the two-phase interface represent characteristic features of early-stage shock–liquid-column interaction. They appear as discontinuities of varying intensity, posing significant challenges for numerical modelling. The liquid column subsequently flattens in the flow direction and expanding in the transverse direction. As further quantitative validation, figure 18 shows the evolution of the width of the column W along the centreline, compared with experiments and numerical simulations as reported in Reyhanian *et al.* (2020) for three Mach numbers. The results are in good agreement with both the experiments and simulations showing that the deformation of the liquid column was accurately captured by the proposed scheme.

In addition to the flow features discussed above, we examine the thermodynamic states sampled by the solution. Unlike previously documented configurations, the present case evolves near the critical point. Figure 19 shows the thermodynamic state at $t/t_0 = 0.3$. Along the centreline, from left to right, the fluid first occupies the post-shock vapour state labelled PSV, which lies above both the critical pressure and the critical-temperature isotherm and is therefore supercritical. Behind the reflected shock, the pressure and temperature increase sharply, with the pressure reaching nearly twice the critical value. Across the liquid-column interface, the pressure remains approximately constant while the temperature decreases. This brings the fluid below the critical-temperature isotherm to the state labelled PSL. Inside the liquid column, the shock reduces both pressure and temperature, driving the fluid toward the saturated liquid state. Overall, the shock interaction heats the initially saturated liquid column to temperatures close to, but slightly below, the critical temperature, while the surrounding vapour is driven well above it. The resulting configuration is a supercritical vapour surrounding in contact with a marginally subcritical liquid column.

https://doi.org/10.1017/jfm.2026.11636 Published online by Cambridge University Press

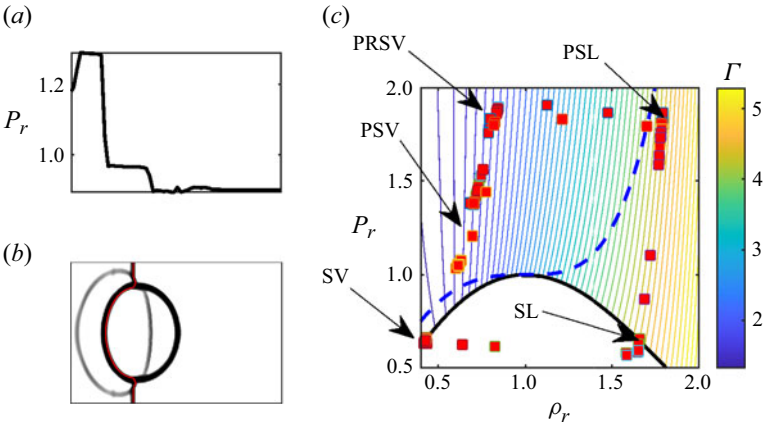


Figure 19. Shock–liquid-column interaction for $Ma = 1.47$ at $t/t_0 = 0.3$. (Bottom left) numerical Schlieren image. (*a*) reduced pressure distribution along the x-axis centreline. (*b*) Fundamental derivative iso-contours in P_r–ρ_r plane. Red square symbols represent the state of the domain. The blue dash lined is the critical-temperature isotherm. Solid black line is the co-existence curve; PSV: post-shock vapour, PRSV: post-reflected shock vapour, PSL: post-shock liquid, SL: saturated liquid and SV: saturated vapour.

5. Conclusion

The development of numerical methods for compressible non-ideal fluid dynamics remains comparatively underexplored, despite the growing relevance of such flows in modern energy systems. In this work, we have proposed a kinetic framework and its lattice Boltzmann realisation specifically designed to address this gap.

At the core of the approach lies a thermodynamically consistent kinetic model for dense fluids, based on two BGK-type collision operators with Gaussian attractors defined by a local reference state and a shifted equilibrium. This construction enables the incorporation of the full non-ideal thermodynamic pressure as the local reference attractor while accounting for the inherently non-local nature of intermolecular interactions. In contrast to formulations relying on a single BGK operator carrying the full pressure – which may lead to non-physical behaviour such as non-positive bulk viscosity and density-gradient-dependent energy diffusion in the heat flux – the present model ensures positive-definite transport properties and recovers the target macroscopic balance equations under appropriate scaling.

We then developed a consistent lattice Boltzmann discretisation yielding a second-order accurate numerical scheme. The resulting model was validated across a range of canonical configurations. In particular, shock-tube simulations revealed the emergence of non-classical wave dynamics, including rarefaction shocks and mixed rarefaction fan–shock structures associated with regions of negative fundamental derivative. Simulations of a shock wave interacting with a liquid column near critical conditions further demonstrated the ability of the model to capture strong thermodynamic effects, such as shock-induced transitions toward supercritical states. In the shock–liquid-column interaction case, the initially saturated liquid column experiences a strong temperature rise following shock impact. The liquid-column temperature approaches the critical value, while the surrounding vapour exceeds it, resulting in a marginally subcritical liquid column, surrounded by a supercritical vapour.

In the hydrodynamic limit, corresponding to the long-wavelength limit, both the kinetic formulation and its lattice Boltzmann discretisation are stable for arbitrary parameter choices. For finite wavenumbers, which are present in most practical simulations and

https://doi.org/10.1017/jfm.2026.11636 Published online by Cambridge University Press

particularly in strongly compressible configurations such as shock tubes, a practical stability condition commonly observed in third-order quadrature-based schemes is $\theta < \delta x^2/(3\delta t^2)$. This constraint appears largely independent of the particular collision operator employed. In addition, regimes where β approaches unity may lead to numerical oscillations due to the increasing influence of higher-order kinetic moments. In principle, such effects can be mitigated using multiple-relaxation-time collision models, which allow improved control over higher-order moments such as the entropic multiple-relaxation-time collision operator (Karlin, Bösch & Chikatamarla 2014). This will be addressed in upcoming publications.

Overall, the results highlight the capability of the proposed framework to reproduce key non-ideal compressible phenomena within an efficient kinetic formulation. The thermodynamic consistency and robustness of the model make it a promising tool for the investigation of complex flows involving strong departures from ideal-gas behaviour, including regimes relevant to supercritical technologies and phase-transition-driven processes such as flash boiling.

Acknowledgements. The authors would like to thank P. Jenny for support and fruitful discussions.

Funding. This work was supported by European Research Council (ERC) Advanced Grant No. 834763-PonD and by the Swiss National Science Foundation (SNSF) Grants 200021-228065 and 200021-236715. Computational resources at the Swiss National Super computing Center (CSCS) were provided under Grants No. s1286, sm101 and s1327. Authors would like to thank Patrick Jenny for his support and fruitful discussions.

Declaration of interests. The authors report that they do not have a conflict of interest.

Data availability statement. The data that support the findings of this study are available from the corresponding author upon request.

Appendix A. Multi-scale analysis of kinetic model

To derive the hydrodynamic limit of the kinetic model, we consider the time-evolution equations

$$\partial_t\{f,g\} + \boldsymbol{v}\cdot\boldsymbol{\nabla}\{f,g\} = \frac{1}{\tau}\left(\left\{f^{eq},g^{eq}\right\} - \{f,g\}\right) + \frac{1}{\lambda}\left(\left\{f^{\star}_{\lambda},g^{\star}_{\lambda}\right\} - \left\{f^{eq},g^{eq}\right\}\right). \quad \text{(A1)}$$

For clarity, we restrict attention to the limit $\lambda \to 0$. In this limit, the shifted-equilibrium operators reduce to

$$\lim_{\lambda\to 0}\frac{1}{\lambda}\left(\left\{f^{\star}_{\lambda},g^{\star}_{\lambda}\right\} - \left\{f^{eq},g^{eq}\right\}\right) = \left\{\mathcal{F}^{\star},\mathcal{G}^{\star}\right\}, \quad \text{(A2)}$$

where

$$\mathcal{F}^{\star} = \left[\frac{\boldsymbol{F}\cdot(\boldsymbol{v}-\boldsymbol{u})}{P} + \alpha(\boldsymbol{\nabla}\cdot\boldsymbol{u})\left(\frac{\rho(\boldsymbol{v}-\boldsymbol{u})^2}{2P} - \frac{D}{2}\right)\right] f^{eq}, \quad \text{(A3)}$$

$$\mathcal{G}^{\star} = \left(\frac{\boldsymbol{v}^2}{2} + e(\rho,T) - \frac{DP}{2\rho}\right)\mathcal{F}^{\star} + \frac{(\boldsymbol{v}-\boldsymbol{u})\cdot\boldsymbol{q}^c}{P} f^{eq}, \quad \text{(A4)}$$

with

$$\boldsymbol{q}^c = P\left(\boldsymbol{\nabla}h - \frac{k}{\mu}\boldsymbol{\nabla}T\right). \quad \text{(A5)}$$

We next introduce a non-dimensional formulation based on the characteristic scales

(i) flow velocity $\mathcal{U}$;
(ii) length scale $\mathcal{L}$;

https://doi.org/10.1017/jfm.2026.11636 Published online by Cambridge University Press

(iii) time scale $\mathcal{T} = \mathcal{L}/\mathcal{U}$;
(iv) reference density $\bar{\rho}$;
(v) speed of sound c_s (see (2.17));
(vi) interface thickness δ.

The corresponding dimensionless variables are defined as

(i) $t = \mathcal{T} t'$;
(ii) $\boldsymbol{x} = \mathcal{L}\boldsymbol{x}'$;
(iii) $\boldsymbol{u} = \mathcal{U}\boldsymbol{u}'$;
(iv) $\boldsymbol{v} = c_s \boldsymbol{v}'$;
(v) $\rho = \bar{\rho}\rho'$;
(vi) $f = \bar{\rho} c_s^{-3} f'$;
(vii) $g = \bar{\rho} c_s^{-1} g'$.

This introduces the following dimensionless groups:

(i) Knudsen number $Kn = \tau c_s/\mathcal{L}$;
(ii) Mach number $Ma = \mathcal{U}/c_s$;
(iii) Cahn number $Ca = \delta/\mathcal{L}$.

The dimensionless evolution equations then read

$$\partial_t' f' + \frac{1}{Ma}\boldsymbol{v}' \cdot \nabla' f' = \frac{1}{MaKn}\left((f^{eq})' - f'\right) + \left[\frac{Ca^2}{Ma}\frac{\boldsymbol{F}' \cdot (\boldsymbol{v}' - \boldsymbol{u}')}{P'} + \frac{1}{Ma}\alpha'(\nabla' \cdot \boldsymbol{u}')\left(\frac{\rho'(\boldsymbol{v}' - \boldsymbol{u}')^2}{2P'} - \frac{D}{2}\right)\right](f^{eq})', \tag{A6}$$

and

$$\partial_t' g' + \frac{1}{Ma}\boldsymbol{v}' \cdot \nabla' g' = \frac{1}{MaKn}\left((g^{eq})' - g'\right) + \frac{1}{Ma}\frac{(\boldsymbol{v}' - \boldsymbol{u}') \cdot \boldsymbol{q}^{c\prime}}{P'}(f^{eq})' + \left[\frac{Ca^2}{Ma}\frac{\boldsymbol{F}' \cdot (\boldsymbol{v}' - \boldsymbol{u}')}{P'} + \frac{1}{Ma}\alpha'(\nabla' \cdot \boldsymbol{u}')\left(\frac{\rho'(\boldsymbol{v}' - \boldsymbol{u}')^2}{2P'} - \frac{D}{2}\right)\right](g^{eq})'. \tag{A7}$$

Finally, we adopt the scaling assumptions

(i) acoustic scaling $Ma \sim O(1)$;
(ii) hydrodynamic scaling $Kn \sim \epsilon$;
(iii) capillary scaling $Ca \sim O(1)$.

Under these assumptions, the system reduces to

$$\epsilon\left(\partial_t\{f, g\} + \boldsymbol{v} \cdot \nabla\{f, g\}\right) = \left(\{f^{eq}, g^{eq}\} - \{f, g\}\right) + \{\mathcal{F}^\star, \mathcal{G}^\star\}, \tag{A8}$$

where primes have been omitted for clarity.

To probe the hydrodynamic limit, $\epsilon \to 0$, we introduce a multi-scale expansion in terms of the smallness parameter ϵ

$$\{f, g\} = \{f^{(0)}, g^{(0)}\} + \epsilon\{f^{(1)}, g^{(1)}\} + \epsilon^2\{f^{(2)}, g^{(2)}\} + \mathcal{O}(\epsilon^3), \tag{A9}$$

$$\{\mathcal{F}^\star, \mathcal{G}^\star\} = \epsilon\{\mathcal{F}^{\star(1)}, \mathcal{G}^{\star(1)}\}, \tag{A10}$$

https://doi.org/10.1017/jfm.2026.11636 Published online by Cambridge University Press

Moment	f^{eq}	g^{eq}
1	ρ	ρE
v_α	ρu_α	$\rho(E+P/\rho)u_\alpha$
$v_\alpha v_\beta$	$\rho u_\alpha u_\beta + P\delta_{\alpha\beta}$	$\rho u_\alpha u_\beta(E+2P/\rho) + P(E+P/\rho)\delta_{\alpha\beta}$
$v_\alpha v_\beta v_\gamma$	$\rho u_\alpha u_\beta u_\gamma + P(u_\alpha\delta_{\beta\gamma} + u_\beta\delta_{\alpha\gamma} + u_\gamma\delta_{\alpha\beta})$	—

Table 5. Moments of f^{eq} and g^{eq}.

Moment	$\mathcal{F}^\star$	$\mathcal{G}^\star$
1	0	$\boldsymbol{u}\cdot\boldsymbol{F}$
v_α	F_α	$u_\alpha(\boldsymbol{u}\cdot\boldsymbol{F}) + q^c_\alpha$
$v_\alpha v_\beta$	$u_\alpha F_\beta + u_\beta F_\alpha + P\alpha(\boldsymbol{\nabla}\cdot\boldsymbol{u})$	$(u_\alpha u_\beta + \delta_{\alpha\beta}(P/\rho))(\boldsymbol{u}\cdot\boldsymbol{F}) + (P/\rho)(u_\alpha(F_\beta + (\rho q^c_\beta/P)) + u_\beta(F_\alpha + (\rho q^c_\alpha/P)))$

Table 6. Moments of $\mathcal{F}^\star$ and $\mathcal{G}^\star$.

and

$$\partial_t = \partial_t^{(1)} + \epsilon\partial_t^{(2)} + +\mathcal{O}(\epsilon^3), \tag{A11}$$

into the dimensional equations and separate in terms of different orders of ϵ

$$\epsilon^0:\ 0 = \frac{1}{\tau}\left(\{f^{eq}, g^{eq}\} - \{f^{(0)}, g^{(0)}\}\right), \tag{A12}$$

$$\epsilon^1:\ \partial_t^{(1)}\{f^{(0)}, g^{(0)}\} + \boldsymbol{v}\cdot\boldsymbol{\nabla}\{f^{(0)}, g^{(0)}\} = -\frac{1}{\tau}\{f^{(1)}, g^{(1)}\} + \{\mathcal{F}^{\star(1)}, \mathcal{G}^{\star(1)}\}, \tag{A13}$$

$$\epsilon^2:\ \partial_t^{(1)}\{f^{(1)}, g^{(1)}\} + \boldsymbol{v}\cdot\boldsymbol{\nabla}\{f^{(1)}, g^{(1)}\} + \partial_t^{(2)}\{f^{(0)}, g^{(0)}\} = -\frac{1}{\tau}\{f^{(2)}, g^{(2)}\} + \{\mathcal{F}^{\star(2)}, \mathcal{G}^{\star(2)}\}. \tag{A14}$$

From order ϵ^0 it directly follows that

$$\{f^{(0)}, g^{(0)}\} = \{f^{eq}, g^{eq}\}. \tag{A15}$$

Before moving on to the next orders, for the sake of readability we have listed the moments of f^{eq}, g^{eq}, $\mathcal{F}^\star$ and $\mathcal{G}^\star$ in tables 5 and 6.

Next, going to order ϵ and computing the moments $\int\{f, \boldsymbol{v}f, g\}\mathrm{d}\boldsymbol{v}$ of the Chapman–Enskog-expanded equations, using solvability conditions

$$\int m\{1, \boldsymbol{v}\}f^{(k)}\mathrm{d}\boldsymbol{v} = 0,\ \forall k > 0, \tag{A16}$$

$$\int m g^{(k)}\mathrm{d}\boldsymbol{v} = 0,\ \forall k > 0, \tag{A17}$$

and the moments listed in tables 5 and 6 we obtain

$$\partial_t^{(1)}\rho + \boldsymbol{\nabla}\cdot\rho\boldsymbol{u} = 0, \tag{A18}$$

$$\partial_t^{(1)}(\rho\boldsymbol{u}) + \boldsymbol{\nabla}\cdot(\rho\boldsymbol{u}\otimes\boldsymbol{u} + P\boldsymbol{I}) = -\boldsymbol{\nabla}\cdot\boldsymbol{T}_K, \tag{A19}$$

$$\partial_t^{(1)}(\rho E) + \boldsymbol{\nabla}\cdot(\rho E\boldsymbol{u} + P\boldsymbol{u}) = -\boldsymbol{u}\cdot\boldsymbol{\nabla}\cdot\boldsymbol{T}_K. \tag{A20}$$

https://doi.org/10.1017/jfm.2026.11636 Published online by Cambridge University Press

The last equation, (A20), can be transformed into a balance equation for internal energy using

$$\partial_t^{(1)}\mathcal{K} + \boldsymbol{\nabla}\cdot(\boldsymbol{u}\mathcal{K}) + \boldsymbol{u}\cdot\boldsymbol{\nabla}P + \boldsymbol{u}\cdot\boldsymbol{\nabla}\cdot\boldsymbol{T}_K = 0, \tag{A21}$$

as

$$\partial_t^{(1)}\rho e + \boldsymbol{\nabla}\cdot\rho\boldsymbol{u}e + P\boldsymbol{\nabla}\cdot\boldsymbol{u} = 0. \tag{A22}$$

Furthermore, using

$$\mathrm{d}e = c_v\mathrm{d}T - \left(T\left(\frac{\partial P}{\partial T}\right)_\rho - P\right)\frac{\mathrm{d}\rho}{\rho^2}, \tag{A23}$$

and (A18) a balance equation for temperature can be derived as

$$\partial_t^{(1)}T + \boldsymbol{u}\cdot\boldsymbol{\nabla}T + \frac{T}{\rho c_v}\left(\frac{\partial P}{\partial T}\right)_\rho \boldsymbol{\nabla}\cdot\boldsymbol{u} = 0. \tag{A24}$$

Finally, using

$$\mathrm{d}P = \left(\frac{\partial P}{\partial \rho}\right)_T \mathrm{d}\rho + \left(\frac{\partial P}{\partial T}\right)_\rho \mathrm{d}T, \tag{A25}$$

we can also write a balance equation for pressure as

$$\partial_t^{(1)}P + \boldsymbol{u}\cdot\boldsymbol{\nabla}P + \rho c_s^2\boldsymbol{\nabla}\cdot\boldsymbol{u} = 0, \tag{A26}$$

where

$$c_s^2 = \left(\frac{\partial P}{\partial \rho}\right)_T + \frac{T}{c_v\rho^2}\left(\frac{\partial P}{\partial T}\right)_\rho^2. \tag{A27}$$

At order ϵ^2, the continuity equation becomes

$$\partial_t^{(2)}\rho = 0, \tag{A28}$$

while for the momentum balance equation one has

$$\partial_t^{(2)}(\rho\boldsymbol{u}) + \boldsymbol{\nabla}\cdot\int \boldsymbol{v}\otimes\boldsymbol{v}f^{(1)}\mathrm{d}\boldsymbol{v} = 0. \tag{A29}$$

The second term can be expanded using the first-order-in-ϵ equation, as

$$-\frac{1}{\tau}\int \boldsymbol{v}\otimes\boldsymbol{v}f^{(1)}\mathrm{d}\boldsymbol{v} + \int \boldsymbol{v}\otimes\boldsymbol{v}\mathcal{F}^{\star(1)}\mathrm{d}\boldsymbol{v} = \partial_t^{(1)}\int \boldsymbol{v}\otimes\boldsymbol{v}f^{(0)}\mathrm{d}\boldsymbol{v} + \boldsymbol{\nabla}\cdot\int \boldsymbol{v}\otimes\boldsymbol{v}\otimes\boldsymbol{v}f^{(0)}\mathrm{d}\boldsymbol{v}, \tag{A30}$$

where

$$\partial_t^{(1)}\int \boldsymbol{v}\otimes\boldsymbol{v}f^{(0)}\mathrm{d}\boldsymbol{v} = \partial_t^{(1)}(\rho\boldsymbol{u}\otimes\boldsymbol{u} + P\boldsymbol{I}), \tag{A31}$$

$$\boldsymbol{\nabla}\cdot\int \boldsymbol{v}\otimes\boldsymbol{v}\otimes\boldsymbol{v}f^{(0)}\mathrm{d}\boldsymbol{v} = \boldsymbol{\nabla}\cdot(\rho\boldsymbol{u}\otimes\boldsymbol{u}\otimes\boldsymbol{u}) + \boldsymbol{\nabla}(P\boldsymbol{u}) + \boldsymbol{\nabla}(P\boldsymbol{u})^\dagger + \boldsymbol{\nabla}\cdot(P\boldsymbol{u}), \tag{A32}$$

$$\int \boldsymbol{v}\otimes\boldsymbol{v}\mathcal{F}^{\star(1)}\mathrm{d}\boldsymbol{v} = \lambda(\boldsymbol{u}\otimes\boldsymbol{F} + \boldsymbol{F}\otimes\boldsymbol{u}) + \frac{P}{\rho}\left(\frac{D+2}{D} - \frac{\rho c_s^2}{P} - \frac{\eta}{\mu}\right)(\boldsymbol{\nabla}\cdot\boldsymbol{u}), \tag{A33}$$

https://doi.org/10.1017/jfm.2026.11636 Published online by Cambridge University Press

The time derivative term can be expanded as

$$\partial_t^{(1)}\left(\rho \boldsymbol{u}\otimes\boldsymbol{u}+P\boldsymbol{I}\right)=\boldsymbol{u}\otimes\partial_t^{(1)}\rho\boldsymbol{u}+\left(\boldsymbol{u}\otimes\partial_t^{(1)}\rho\boldsymbol{u}\right)^{\dagger}-\boldsymbol{u}\otimes\boldsymbol{u}\partial_t^{(1)}\rho+\partial_t^{(1)}P\boldsymbol{I}, \tag{A34}$$

which then using Euler level balance equations, (A18), (A19) and (A26), yields

$$\begin{aligned}\partial_t^{(1)}\left(\rho \boldsymbol{u}\otimes\boldsymbol{u}+P\boldsymbol{I}\right)=&-\boldsymbol{u}\otimes\left[\nabla\cdot\rho\boldsymbol{u}\otimes\boldsymbol{u}+\nabla P+\boldsymbol{F}\right]-\left(\boldsymbol{u}\otimes\left[\nabla\cdot\rho\boldsymbol{u}\otimes\boldsymbol{u}+\nabla P+\boldsymbol{F}\right]\right)^{\dagger}\\&+\boldsymbol{u}\otimes\boldsymbol{u}\nabla\cdot\rho\boldsymbol{u}-(\nabla\cdot P\boldsymbol{u})\boldsymbol{I}+\left(P-\rho c_s^2\right)(\nabla\cdot\boldsymbol{u})\boldsymbol{I}.\end{aligned} \tag{A35}$$

Adding contributions from other terms

$$\int \boldsymbol{v}\otimes\boldsymbol{v}f^{(1)}\mathrm{d}\boldsymbol{v}=-\tau P\left[\nabla\boldsymbol{u}+\nabla\boldsymbol{u}^{\dagger}+\left(\frac{\eta}{\mu}-\frac{2}{D}\right)(\nabla\cdot\boldsymbol{u})\boldsymbol{I}\right]. \tag{A36}$$

Plugging this final expression into the momentum balance equation at order ϵ^2, and setting $\tau=\mu/P$, results in

$$\partial_t^{(2)}(\rho\boldsymbol{u})+\nabla\cdot\boldsymbol{T}_{NS}=0. \tag{A37}$$

For the energy balance at order ϵ^2

$$\partial_t^{(2)}\rho E+\nabla\cdot\int\boldsymbol{v}g^{(1)}\mathrm{d}\boldsymbol{v}=0, \tag{A38}$$

which can be evaluated using the order ϵ as

$$-\frac{1}{\tau}\int\boldsymbol{v}g^{(1)}\mathrm{d}\boldsymbol{v}+\int\boldsymbol{v}\mathcal{G}^{\star(1)}\mathrm{d}\boldsymbol{v}=\partial_t^{(1)}\int\boldsymbol{v}g^{(0)}\mathrm{d}\boldsymbol{v}+\nabla\cdot\int\boldsymbol{v}\otimes\boldsymbol{v}g^{(0)}\mathrm{d}\boldsymbol{v}, \tag{A39}$$

where

$$\partial_t^{(1)}\int\boldsymbol{v}g^{(0)}\mathrm{d}\boldsymbol{v}=\partial_t^{(1)}\left(\rho E\boldsymbol{u}+P\boldsymbol{u}\right), \tag{A40}$$

$$\nabla\cdot\int\boldsymbol{v}\otimes\boldsymbol{v}g^{(0)}\mathrm{d}\boldsymbol{v}=\nabla\cdot\left(\boldsymbol{u}\otimes\boldsymbol{u}(\rho E+P)+(E+P/\rho)P\boldsymbol{I}\right), \tag{A41}$$

$$\begin{aligned}\int\boldsymbol{v}\mathcal{G}^{\star(1)}\mathrm{d}\boldsymbol{v}=&\left(\boldsymbol{u}(\boldsymbol{u}\cdot\boldsymbol{F})+\boldsymbol{F}(E+P/\rho)\right)+P\boldsymbol{u}\left(\frac{D+2}{D}-\frac{\rho c_s^2}{P}-\frac{\eta}{\mu}\right)(\nabla\cdot\boldsymbol{u})\\&+P\left(\nabla h-\frac{k}{\mu}\nabla T\right).\end{aligned} \tag{A42}$$

Adding these terms up and using balance equations for $P\boldsymbol{u}$ and $\rho E\boldsymbol{u}$

$$\partial_t^{(1)}P\boldsymbol{u}+\nabla\cdot P\boldsymbol{u}\otimes\boldsymbol{u}+\frac{P}{\rho}\nabla P+\frac{P}{\rho}\nabla\cdot\boldsymbol{T}_K+\boldsymbol{u}\left(\rho c_s^2-P\right)\nabla\cdot\boldsymbol{u}=0, \tag{A43}$$

and

$$\partial_t^{(1)}\rho E\boldsymbol{u}+\nabla\cdot(\rho E+P)\boldsymbol{u}\otimes\boldsymbol{u}+E\nabla P+E\nabla\cdot\boldsymbol{T}_K-P\boldsymbol{u}\cdot\nabla\boldsymbol{u}+\boldsymbol{u}(\boldsymbol{u}\cdot\nabla\cdot\boldsymbol{T}_K)=0, \tag{A44}$$

we eventually recover

$$\partial_t^{(2)}\rho E+\nabla\cdot\boldsymbol{u}\cdot\boldsymbol{T}_{NS}-\nabla\cdot k\nabla T=0. \tag{A45}$$

https://doi.org/10.1017/jfm.2026.11636 Published online by Cambridge University Press

Appendix B. Second-order-in-time discretisation

We follow a procedure first introduced by He *et al.* (1998) to discretised the kinetic models introduced here

$$\partial_t f + \boldsymbol{v}\cdot\nabla f = -\frac{1}{\tau}(f - f^{eq}) + \frac{1}{\lambda}(f^{\star}_{\lambda} - f^{eq}), \tag{B1}$$

$$\partial_t g + \boldsymbol{v}\cdot\nabla g = -\frac{1}{\tau}(g - g^{eq}) + \frac{1}{\lambda}(g^{\star}_{\lambda} - g^{eq}). \tag{B2}$$

The main ingredient in space/time discretisation is the integration along characteristics, here the velocities $\boldsymbol{v}$, over a time δt, which leads to

$$f(\boldsymbol{x}+\boldsymbol{v}\delta t, t+\delta t) - f(\boldsymbol{x}, t) = \int_t^{t+\delta t} \left[\frac{1}{\tau}\left(f^{eq} - f\right) + \frac{1}{\lambda}(f^{\star}_{\lambda} - f^{eq})\right] \mathrm{d}t', \tag{B3}$$

$$g(\boldsymbol{x}+\boldsymbol{v}\delta t, t+\delta t) - g(\boldsymbol{x}, t) = \int_t^{t+\delta t} \left[\frac{1}{\tau}\left(g^{eq} - g\right) + \frac{1}{\lambda}(g^{\star}_{\lambda} - g^{eq})\right] \mathrm{d}t'. \tag{B4}$$

The integrals on the right-hand sides are approximated using a trapezoidal rule

$$\begin{aligned}\int_t^{t+\delta t} \left[\frac{1}{\tau}\left(f^{eq} - f\right) + \frac{1}{\lambda}(f^{\star}_{\lambda} - f^{eq})\right] \mathrm{d}t' = {} & \frac{\delta t}{2\tau}\left(f^{eq}(\boldsymbol{x}, t) - f(\boldsymbol{x}, t)\right) \\ & + \frac{\delta t}{2\lambda}\left(f^{\star}_{\lambda}(\boldsymbol{x}, t) - f^{eq}(\boldsymbol{x}, t)\right) \\ & + \frac{\delta t}{2\tau}\big(f^{eq}(\boldsymbol{x}+\boldsymbol{v}\delta t, t+\delta t) \\ & - f(\boldsymbol{x}+\boldsymbol{v}\delta t, t+\delta t)\big) \\ & + \frac{\delta t}{2\lambda}\big(f^{\star}_{\lambda}(\boldsymbol{x}+\boldsymbol{v}\delta t, t+\delta t) \\ & - f^{eq}(\boldsymbol{x}+\boldsymbol{v}_i\delta t, t+\delta t)\big) + \mathcal{O}(\delta t^3).\end{aligned} \tag{B5}$$

A similar equation can be written for g, which we will omit for the sake of readability. The resulting system is implicit in time. To remove the implicitness, the following transformation of variables is introduced (He *et al.* 1998):

$$\bar{f}(\boldsymbol{x}, t) = f(\boldsymbol{x}, t) - \frac{\delta t}{2\tau}\left(f^{eq}(\boldsymbol{x}, t) - f(\boldsymbol{x}, t)\right) - \frac{\delta t}{2\lambda}\left(f^{\star}_{\lambda}(\boldsymbol{x}, t) - f^{eq}(\boldsymbol{x}, t)\right), \tag{B6}$$

$$\bar{g}(\boldsymbol{x}, t) = g(\boldsymbol{x}, t) - \frac{\delta t}{2\tau}\left(g^{eq}(\boldsymbol{x}, t) - g(\boldsymbol{x}, t)\right) - \frac{\delta t}{2\lambda}\left(g^{\star}_{\lambda}(\boldsymbol{x}, t) - g^{eq}(\boldsymbol{x}, t)\right). \tag{B7}$$

Introducing this transformation back into the integrated time-evolution equations

$$\begin{aligned}\bar{f}(\boldsymbol{x}+\boldsymbol{v}\delta t, t+\delta t) = {} & \bar{f}(\boldsymbol{x}, t) + 2\beta\left(f^{eq}(\boldsymbol{x}, t) - \bar{f}(\boldsymbol{x}, t)\right) \\ & + \frac{\delta t}{\lambda}(1-\beta)\left(f^{\star}_{\lambda}(\boldsymbol{x}, t) - f^{eq}(\boldsymbol{x}, t)\right),\end{aligned} \tag{B8}$$

$$\begin{aligned}\bar{g}(\boldsymbol{x}+\boldsymbol{v}\delta t, t+\delta t) = {} & \bar{g}(\boldsymbol{x}, t) + 2\beta\left(g^{eq}(\boldsymbol{x}, t) - \bar{g}(\boldsymbol{x}, t)\right) \\ & + \frac{\delta t}{\lambda}(1-\beta)\left(g^{\star}_{\lambda}(\boldsymbol{x}, t) - g^{eq}(\boldsymbol{x}, t)\right),\end{aligned} \tag{B9}$$

where $\beta \in [0, 1]$ is the relaxation parameter

$$\beta = \frac{\delta t}{2\tau + \delta t}. \tag{B10}$$

https://doi.org/10.1017/jfm.2026.11636 Published online by Cambridge University Press

The final step is to evaluate moments of the distribution function that are needed to define $\{f^{eq}, g^{eq}\}$ and $\{f_\lambda^\star, g_\lambda^\star\}$ using the transformed distribution functions $\{\bar{f}, \bar{g}\}$. Integrating over $\{\bar{f}, \bar{g}\}$ and using the definitions for the transformed variables it is readily shown that

$$\int m\bar{f}\,\mathrm{d}\boldsymbol{v} = \int mf\,\mathrm{d}\boldsymbol{v} = \rho, \tag{B11}$$

$$\int m\boldsymbol{v}\bar{f}\,\mathrm{d}\boldsymbol{v} = \int m\boldsymbol{v}\left(f - \frac{\delta t}{2\lambda}\left(f_\lambda^\star - f^{eq}\right)\right)\mathrm{d}\boldsymbol{v} = \rho\boldsymbol{u} - \frac{\delta t}{2}\boldsymbol{F}, \tag{B12}$$

$$\int m\bar{g}\,\mathrm{d}\boldsymbol{v} = \int m\left(g - \frac{\delta t}{2\lambda}\left(g_\lambda^\star - g^{eq}\right)\right)\mathrm{d}\boldsymbol{v} = \rho E - \frac{\delta t}{2}\boldsymbol{u}\cdot\boldsymbol{F}. \tag{B13}$$

This completes the integration along characteristics of the kinetic model. Renaming the variables $\{\bar{f}, \bar{g}\} \to \{f, g\}$ and dropping the dependence on the untransformed distribution function, we obtain the second-order-in-time accurate kinetic (3.26) and (3.27) of the main text, along with the corresponding transform of the fields, (3.29), (3.30) and (3.31).

Appendix C. Multi-scale analysis of lattice Boltzmann model for compressible non-ideal flows

The first step in the multi-scale analysis is a Taylor expansion of the lattice Boltzmann equations

$$\begin{aligned}\{f_i, g_i\}(\boldsymbol{x} + \boldsymbol{c}_i\delta t, t + \delta t) = \{f_i, g_i\}(\boldsymbol{x}, t) + 2\beta\left(\left\{f_i^{eq}, g_i^{eq}\right\}(\boldsymbol{x}, t) - \{f_i, g_i\}(\boldsymbol{x}, t)\right)\\ + (1-\beta)\left(\left\{f_i^\star, g_i^\star\right\}(\boldsymbol{x}, t) - \left\{f_i^{eq}, g_i^{eq}\right\}(\boldsymbol{x}, t)\right),\end{aligned} \tag{C1}$$

around $(\boldsymbol{x}, t)$, leading to the following space- and time-evolution equations:

$$\begin{aligned}\delta t\mathcal{D}_t\{f_i, g_i\} + \frac{\delta t^2}{2}\mathcal{D}_t{}^2\{f_i, g_i\} + \mathcal{O}\left(\delta t^3\right) = 2\beta\left(\left\{f_i^{eq}, g_i^{eq}\right\} - \{f_i, g_i\}\right)\\ + (1-\beta)\left(\left\{f_i^\star, g_i^\star\right\} - \left\{f_i^{eq}, g_i^{eq}\right\}\right).\end{aligned} \tag{C2}$$

Introducing the flow characteristic size and time, $\mathcal{L}$ and $\mathcal{T}$. The equations are made non-dimensional as

$$\begin{aligned}\frac{\delta x}{\mathcal{L}}\mathcal{D}_t'\{f_i, g_i\} + \frac{\delta x^2}{2\mathcal{L}^2}\mathcal{D}_t'{}^2\{f_i, g_i\} = 2\beta\left(\{f_i^{eq}, g_i^{eq}\} - \{f_i, g_i\}\right)\\ + (1-\beta)\left(\left\{f_i^\star, g_i^\star\right\} - \{f_i^{eq}, g_i^{eq}\}\right),\end{aligned} \tag{C3}$$

where

$$\mathcal{D}_t' = \frac{\mathcal{L}/\mathcal{T}}{\delta x/\delta t}\left(\partial_t' + \boldsymbol{c}_i'\cdot\boldsymbol{\nabla}'\right). \tag{C4}$$

Assuming acoustic scaling and hydrodynamic scaling, $\varepsilon \sim \delta x/\mathcal{L} \sim \delta t/\mathcal{T}$ and dropping the primes

$$\begin{aligned}\varepsilon\mathcal{D}_t\{f_i, g_i\} + \frac{\varepsilon^2}{2}\mathcal{D}_t{}^2\{f_i, g_i\} = 2\beta\left(\{f_i^{eq}, g_i^{eq}\} - \{f_i, g_i\}\right)\\ + (1-\beta)\left(\{f_i^\star, g_i^\star\} - \{f_i^{eq}, g_i^{eq}\}\right).\end{aligned} \tag{C5}$$

https://doi.org/10.1017/jfm.2026.11636 Published online by Cambridge University Press

We introduce the following multi-scale expansions:

$$f_i = f_i^{(0)} + \varepsilon f_i^{(1)} + \varepsilon^2 f_i^{(2)} + O(\varepsilon^3), \tag{C6a}$$
$$g_i = g_i^{(0)} + \varepsilon g_i^{(1)} + \varepsilon^2 g_i^{(2)} + O(\varepsilon^3), \tag{C6b}$$
$$f_i^\star = f_i^{\star(0)} + \varepsilon f_i^{\star(1)} + \varepsilon^2 f_i^{\star(2)} + O(\varepsilon^3), \tag{C6c}$$
$$g_i^\star = g_i^{\star(0)} + \varepsilon g_i^{\star(1)} + \varepsilon^2 g_i^{\star(2)} + O(\varepsilon^3), \tag{C6d}$$
$$\partial_t = \varepsilon \partial_t^{(1)} + \varepsilon^2 \partial_t^{(2)} + O(\varepsilon^3). \tag{C6e}$$

Noting that for the definition of $f_i^\star$ in (3.45) divergence from the equilibrium will arise only at the ε^1 level (i.e. $f_i^{\star(0)} = f_i^{eq}$), we separate by orders of the smallness parameter

$$\varepsilon^0 : \{f_i^{(0)}, g_i^{(0)}\} = \{f_i^{eq}, g_i^{eq}\}, \tag{C7a}$$
$$\varepsilon : \mathcal{D}_t^{(1)}\{f_i^{(0)}, g_i^{(0)}\} = -2\beta\{f_i^{(1)}, g_i^{(1)}\} + (1-\beta)\{f^{\star}{}_i^{(1)}, g^{\star}{}_i^{(1)}\}, \tag{C7b}$$
$$\varepsilon^2 : \partial_t^{(2)}\{f_i^{(0)}, g_i^{(0)}\} + \mathcal{D}_t^{(1)}(1-\beta)\left(\{f_i^{(1)}, g_i^{(1)}\} + \frac{1}{2}\{f^{\star}{}_i^{(1)}, g^{\star}{}_i^{(1)}\}\right)$$
$$= -2\beta\{f_i^{(2)}, g_i^{(2)}\} + (1-\beta)\{f^{\star}{}_i^{(2)}, g^{\star}{}_i^{(2)}\}. \tag{C7c}$$

The following solvability conditions apply:

$$\sum_{i=1}^{Q} f_i^{(k)} = 0, \ \forall k > 0, \tag{C8}$$
$$\sum_{i=1}^{Q} \boldsymbol{c}_i f_i^{(1)} + \frac{1}{2}\sum_{i=1}^{Q} \boldsymbol{c}_i f^{\star}{}_i^{(1)} = 0, \tag{C9}$$
$$\sum_{i=1}^{Q} \boldsymbol{c}_i f_i^{(k)} = 0, \ \forall k > 1, \tag{C10}$$
$$\sum_{i=1}^{Q} g_i^{(1)} + \frac{1}{2}\sum_{i=1}^{Q} g^{\star}{}_i^{(1)} = 0, \tag{C11}$$
$$\sum_{i=1}^{Q} g_i^{(k)} = 0, \ \forall k > 0. \tag{C12}$$

Taking the zeroth-order moment of (C7*b*) for f_i

$$\partial_t^{(1)}\rho + \boldsymbol{\nabla}\cdot\rho\boldsymbol{u} = 0, \tag{C13}$$

where we have used

$$\sum_{i=1}^{Q} f_i^{\star(1)} = 0, \tag{C14}$$

https://doi.org/10.1017/jfm.2026.11636 Published online by Cambridge University Press

and solvability condition (C8). For the first-order moment of (C7*b*) for f_i

$$\partial_t^{(1)}\rho\boldsymbol{u}+\boldsymbol{\nabla}\cdot\rho\boldsymbol{u}\otimes\boldsymbol{u}+\boldsymbol{\nabla}P=-2\beta\overbrace{\left(\sum_{i=1}^{Q}\boldsymbol{c}_i f_i^{(1)}+\frac{1}{2}\boldsymbol{c}_i f_i^{\star(1)}\right)}^{=0}+\underbrace{\sum_{i=1}^{Q}\boldsymbol{c}_i f_i^{\star(1)}}_{\boldsymbol{F}},\tag{C15}$$

where we used (C9) and

$$\boldsymbol{F}=-\boldsymbol{\nabla}\cdot T_K,\tag{C16}$$

where

$$T_K=\kappa\boldsymbol{\nabla}\rho\otimes\boldsymbol{\nabla}\rho-\kappa\left(\rho\nabla^2\rho+\frac{1}{2}|\boldsymbol{\nabla}\rho|^2\right)\boldsymbol{I}.\tag{C17}$$

The force can also be shown to simplify to

$$\boldsymbol{F}=\kappa\rho\boldsymbol{\nabla}\nabla^2\rho.\tag{C18}$$

Finally taking the zeroth-order moment for g_i

$$\partial_t^{(1)}\rho E+\boldsymbol{\nabla}\cdot\boldsymbol{u}\,(\rho E+P)=-2\beta\overbrace{\left(\sum_{i=1}^{Q}g_i^{(1)}+\frac{1}{2}g_i^{\star(1)}\right)}^{=0}+\underbrace{\sum_{i=1}^{Q}g_i^{\star(1)}}_{\boldsymbol{u}\cdot\boldsymbol{F}}.\tag{C19}$$

Summing up balance equations at order ε

$$\partial_t^{(1)}\rho+\boldsymbol{\nabla}\cdot\rho\boldsymbol{u}=0,\tag{C20}$$

$$\partial_t^{(1)}\rho\boldsymbol{u}+\boldsymbol{\nabla}\cdot(\rho\boldsymbol{u}\otimes\boldsymbol{u}+P\boldsymbol{I})-\boldsymbol{F}=0,\tag{C21}$$

$$\partial_t^{(1)}\rho E+\boldsymbol{\nabla}\cdot\rho\boldsymbol{u}\,(E+P/\rho)-\boldsymbol{u}\cdot\boldsymbol{F}=0.\tag{C22}$$

The last equation (C22) can be transformed into a balance equation for internal energy using

$$\partial_t^{(1)}\mathcal{K}+\boldsymbol{\nabla}\cdot(\boldsymbol{u}\mathcal{K})+\boldsymbol{u}\cdot\boldsymbol{\nabla}P-\boldsymbol{u}\cdot\boldsymbol{F}=0,\tag{C23}$$

as

$$\partial_t^{(1)}\rho e+\boldsymbol{\nabla}\cdot\rho\boldsymbol{u}e+P\boldsymbol{\nabla}\cdot\boldsymbol{u}=0.\tag{C24}$$

Furthermore, using

$$\mathrm{d}e=c_v\mathrm{d}T-\left(T\left(\frac{\partial P}{\partial T}\right)_\rho-P\right)\frac{\mathrm{d}\rho}{\rho^2},\tag{C25}$$

and (C20) a balance equation for temperature can be derived as

$$\partial_t^{(1)}T+\boldsymbol{u}\cdot\boldsymbol{\nabla}T+\frac{T}{\rho c_v}\left(\frac{\partial P}{\partial T}\right)_\rho\boldsymbol{\nabla}\cdot\boldsymbol{u}=0.\tag{C26}$$

Finally, using

$$\mathrm{d}P=\left(\frac{\partial P}{\partial\rho}\right)_T\mathrm{d}\rho+\left(\frac{\partial P}{\partial T}\right)_\rho\mathrm{d}T,\tag{C27}$$

https://doi.org/10.1017/jfm.2026.11636 Published online by Cambridge University Press

we can also write a balance equation for pressure as

$$\partial_t^{(1)} P + \boldsymbol{u}\cdot\nabla P + \rho c_s^2 \nabla\cdot\boldsymbol{u} = 0, \tag{C28}$$

where

$$c_s^2 = \left(\frac{\partial P}{\partial \rho}\right)_T + \frac{T}{c_v \rho^2}\left(\frac{\partial P}{\partial T}\right)_\rho^2. \tag{C29}$$

At order ε^2, the zeroth-order moment of f_i leads to

$$\partial_t^{(2)} \rho = 0, \tag{C30}$$

and the first-order moments

$$\partial_t^{(2)} \rho\boldsymbol{u} + \nabla\cdot(1-\beta)\left[\left(\sum_{i=1}^{Q} \boldsymbol{c}_i\otimes\boldsymbol{c}_i f_i{}^{(1)}\right) + \frac{1}{2}\left(\sum_{i=1}^{Q}\boldsymbol{c}_i\otimes\boldsymbol{c}_i f^{\star(1)}_i\right)\right] = 0. \tag{C31}$$

Here, we can use (C7*b*) to obtain

$$\partial_t^{(2)}\rho\boldsymbol{u} + \nabla\cdot\left(\frac{1}{2}-\frac{1}{2\beta}\right)\left(\partial_t^{(1)}\Pi_2(f^{(0)}) + \nabla\Pi_3(f^{(0)}) - \sum_{i=1}^{Q}\boldsymbol{c}_i\otimes\boldsymbol{c}_i f^{\star(1)}_i\right) = 0. \tag{C32}$$

Here, $\Pi_2^{(0)}(f)$ and $\Pi_3^{(0)}(f)$ are the second- and third-order moment tensors of the equilibrium distribution function

$$\Pi_2(f^{(0)}) = \rho\boldsymbol{u}\otimes\boldsymbol{u} + P\boldsymbol{I}, \tag{C33}$$

$$\Pi_3(f^{(0)}) = \rho\boldsymbol{u}\otimes(\boldsymbol{u}\otimes\boldsymbol{u} + P\boldsymbol{I})\circ(\boldsymbol{1}-\boldsymbol{J}) + 3\rho\varsigma^2\boldsymbol{u}\otimes\boldsymbol{I}\circ\boldsymbol{J}. \tag{C34}$$

Using (C20) and (C21) we can write

$$\partial_t^{(1)}(\rho\boldsymbol{u}\otimes\boldsymbol{u} + P\boldsymbol{I}) = \boldsymbol{u}\otimes\boldsymbol{F} + \boldsymbol{F}\otimes\boldsymbol{u} - \nabla\cdot\rho\boldsymbol{u}\otimes\boldsymbol{u}\otimes\boldsymbol{u} - \nabla P\boldsymbol{u} - (\nabla P\boldsymbol{u})^\dagger + P\left(\nabla\boldsymbol{u} + \nabla\boldsymbol{u}^\dagger\right) + \partial_t^{(1)} P\boldsymbol{I}. \tag{C35}$$

For the last term, i.e. $\partial_t^{(1)} P$, we write a balance equation for P

$$\partial_t^{(1)} P = \left(P - \rho c_s^2\right)\nabla\cdot\boldsymbol{u} - \nabla\cdot P\boldsymbol{u}, \tag{C36}$$

while

$$\nabla\cdot\Pi_3(f^{(0)}) = \left[\nabla\cdot\rho\boldsymbol{u}\otimes\boldsymbol{u}\otimes\boldsymbol{u} + \nabla P\boldsymbol{u} + \nabla P\boldsymbol{u}^\dagger\right] + \rho\Psi + \boldsymbol{I}\nabla\cdot P\boldsymbol{u}, \tag{C37}$$

where

$$\Psi_{\alpha\alpha} = -\frac{1}{\rho}\partial_\alpha u_\alpha\left(u_\alpha^2 + 3\left(P-\rho\varsigma^2\right)\right). \tag{C38}$$

Adding up all the terms

$$\partial_t^{(1)}\Pi_2(f^{(0)}) + \nabla\cdot\Pi_3(f^{(0)}) = \boldsymbol{u}\otimes\boldsymbol{F} + \boldsymbol{F}\otimes\boldsymbol{u} + P\left(\nabla\boldsymbol{u} + \nabla\boldsymbol{u}^\dagger\right) + \left(P-\rho c_s^2\right)\nabla\cdot\boldsymbol{u}\boldsymbol{I} - \rho\Psi. \tag{C39}$$

https://doi.org/10.1017/jfm.2026.11636 Published online by Cambridge University Press

Setting

$$\sum_{i=1}^{Q} \boldsymbol{c}_i \otimes \boldsymbol{c}_i f^{\star(1)}_i = \left(\boldsymbol{u} \otimes \boldsymbol{F} + \boldsymbol{F} \otimes \boldsymbol{u} + \rho \Psi + P \left(\frac{D+2}{D} - \frac{\rho c_s^2}{P} - \frac{\eta}{\mu} \right) \boldsymbol{\nabla} \cdot \boldsymbol{u} \boldsymbol{I} \right), \tag{C40}$$

and plugging it back into (C32)

$$\partial_t^{(2)} \rho \boldsymbol{u} - \boldsymbol{\nabla} \cdot \left[\mu \left(\boldsymbol{\nabla u} + \boldsymbol{\nabla u}^{\dagger} - \frac{2}{D} \boldsymbol{\nabla} \cdot \boldsymbol{u} \boldsymbol{I} \right) + \eta \boldsymbol{\nabla} \cdot \boldsymbol{u} \boldsymbol{I} \right] = 0, \tag{C41}$$

where we used

$$\mu = \left(\frac{1}{2\beta} - \frac{1}{2} \right) P \delta t. \tag{C42}$$

For the second population, at order ε^2,

$$\partial_t^{(2)} \rho E + \boldsymbol{\nabla} \cdot \left(\frac{1}{2} - \frac{1}{2\beta} \right) \left(\partial_t^{(1)} \Pi_1(g_i^{(0)}) + \boldsymbol{\nabla} \cdot \Pi_2(g_i^{(0)}) - \sum_{i=1}^{Q} \boldsymbol{c}_i g_i^{\star(1)} \right) = 0, \tag{C43}$$

where

$$\Pi_1(g_i^{(0)}) = \boldsymbol{u}(\rho E + P), \tag{C44}$$

$$\Pi_2(g_i^{(0)}) = \boldsymbol{u} \otimes \boldsymbol{u} \, (\rho E + 2P) + (E + P/\rho) \, P \boldsymbol{I}. \tag{C45}$$

Here, we can use

$$\partial_t^{(1)} P \boldsymbol{u} + \boldsymbol{\nabla} \cdot P \boldsymbol{u} \otimes \boldsymbol{u} + \frac{P}{\rho} \boldsymbol{\nabla} P - \frac{P}{\rho} \boldsymbol{F} + \boldsymbol{u} \left(\rho c_s^2 - P \right) \boldsymbol{\nabla} \cdot \boldsymbol{u} = 0, \tag{C46}$$

and

$$\partial_t^{(1)} \rho E \boldsymbol{u} + \boldsymbol{\nabla} \cdot (\rho E + P) \boldsymbol{u} \otimes \boldsymbol{u} + E \boldsymbol{\nabla} P - E \boldsymbol{F} - P \boldsymbol{u} \cdot \boldsymbol{\nabla u} - \boldsymbol{u} (\boldsymbol{u} \cdot \boldsymbol{F}) = 0. \tag{C47}$$

Adding up both contributions

$$\begin{aligned} &\partial_t^{(1)} \Pi_1 \left(g_i^{(0)} \right) + \boldsymbol{\nabla} \cdot \Pi_2 \left(g_i^{(0)} \right) \\ &= \underbrace{-2 \boldsymbol{\nabla} \cdot P \boldsymbol{u} \otimes \boldsymbol{u} + 2 \boldsymbol{\nabla} \cdot P \boldsymbol{u} \otimes \boldsymbol{u}}_{=0} \underbrace{+ \boldsymbol{\nabla} \cdot \rho E \boldsymbol{u} \otimes \boldsymbol{u} - \boldsymbol{\nabla} \cdot \rho E \boldsymbol{u} \otimes \boldsymbol{u}}_{=0} \\ &\underbrace{+ \boldsymbol{\nabla} P (P/\rho + E) - (E + P/\rho) \boldsymbol{\nabla} P}_{P \boldsymbol{\nabla} (E + P/\rho)} + P \boldsymbol{u} \cdot \boldsymbol{\nabla u} - \boldsymbol{u} \left(\rho c_s^2 - P \right) \boldsymbol{\nabla} \cdot \boldsymbol{u} \\ &+ (P/\rho + E) \boldsymbol{F} + \boldsymbol{u} (\boldsymbol{u} \cdot \boldsymbol{F}). \end{aligned} \tag{C48}$$

Further expanding

$$\begin{aligned} \partial_t^{(1)} \Pi_1 \left(g_i^{(0)} \right) + \boldsymbol{\nabla} \cdot \Pi_2 \left(g_i^{(0)} \right) = P \boldsymbol{\nabla} h \overbrace{+ P \boldsymbol{\nabla} (\boldsymbol{u}^2/2) + P \boldsymbol{u} \cdot \boldsymbol{\nabla u}}^{= P \boldsymbol{u} \cdot (\boldsymbol{\nabla u} + \boldsymbol{\nabla u}^{\dagger})} + \boldsymbol{u} \left(P - \rho c_s^2 \right) \boldsymbol{\nabla} \cdot \boldsymbol{u} \\ + (P/\rho + E) \boldsymbol{F} + \boldsymbol{u} (\boldsymbol{u} \cdot \boldsymbol{F}), \end{aligned} \tag{C49}$$

https://doi.org/10.1017/jfm.2026.11636 Published online by Cambridge University Press

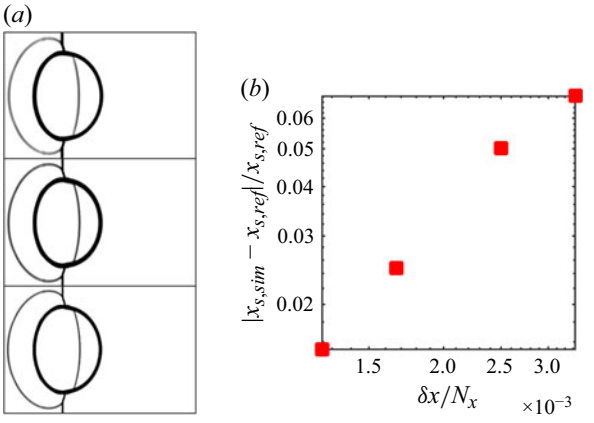


Figure 20. Left: numerical Schlieren image of shock-liquid-column interaction at $Ma = 1.47$ with resolutions (from top to bottom): 600×600, 800×800, 1000×1000. Right: error in position of shock inside the liquid column along the centreline x_s.

where $h = e + P$. Plugging this back into the balance equation

$$\partial_t^{(2)} \rho E - \nabla \cdot \boldsymbol{u} \cdot \underbrace{\left[\mu \left(\nabla \boldsymbol{u} + \nabla \boldsymbol{u} - \frac{2}{D} \nabla \cdot \boldsymbol{u} \boldsymbol{I} \right) + \eta \nabla \cdot \boldsymbol{u} \boldsymbol{I} \right]}_{-\boldsymbol{u} \cdot \boldsymbol{T}_{NS}}$$
$$+ \nabla \cdot \left(\frac{1}{2} - \frac{1}{2\beta} \right) \left(P \nabla h + \boldsymbol{u} \cdot P \left(\frac{D+2}{D} - \frac{\rho c_s^2}{P} - \frac{\eta}{\mu} \right) \nabla \cdot \boldsymbol{u} \boldsymbol{I} \right.$$
$$\left. + (P/\rho + E) \boldsymbol{F} + \boldsymbol{u} (\boldsymbol{u} \cdot \boldsymbol{F}) - \sum_{i=1}^{Q} \boldsymbol{c}_i g_i^{\star(1)} \right) = 0. \tag{C50}$$

Using the definition of the shifted equilibrium

$$\Pi_0(g_i^{\star(1)}) = \boldsymbol{u} \cdot \boldsymbol{F}, \tag{C51}$$
$$\Pi_1(g_i^{\star(1)}) = \left(\boldsymbol{u} (\boldsymbol{u} \cdot \boldsymbol{F}) + \boldsymbol{F} \left(\frac{P}{\rho} + E \right) \right.$$
$$\left. + P \left(\nabla h - \frac{k}{\mu} \nabla T + \boldsymbol{u} \cdot \left(\frac{D+2}{D} - \frac{\rho c_s^2}{P} - \frac{\eta}{\mu} \right) \nabla \cdot \boldsymbol{u} \boldsymbol{I} \right) \right). \tag{C52}$$

we recover

$$\partial_t^{(2)} \rho E + \nabla \cdot \boldsymbol{u} \cdot \boldsymbol{T}_{NS} - \nabla \cdot k \nabla T = 0. \tag{C53}$$

Appendix D. Convergence study of shock–liquid-column interaction

The simulations reported for the shock–column interaction were run with a resolution of 800×800. To check the convergence behaviour for this configuration simulations were run with resolutions from 300×300 up to 1000×1000 using acoustic scaling for the time step. The position of the shock inside the liquid column at $t/t_0 = 0.3$ was then extracted for each run and the relative error with respect to the highest resolution simulation measured. The scaling of this error with resolution along with a visual illustration of the field for $Ma = 1.47$ are shown in figure 20. Fitting the four data points obtained with simulations

https://doi.org/10.1017/jfm.2026.11636 Published online by Cambridge University Press



Figure 21. Distribution of normalised effective viscosity in the domain at $t/t_0 = 0.3$ for $Ma = 1.47$ and resolution of 800×800.

a slope 1.56 was obtained. Note that in all simulations the shock-capturing nonlinear numerical dissipation of (4.37) and (4.39) was on, showing that it does not diminish the overall accuracy of the solver. To better illustrate the operation mode of the numerical dissipation, the normalised effective viscosity in the domain at $t/t_0 = 0.3$ for $Ma = 1.47$ and resolution of 800×800 is shown in figure 21.

References

Ansumali, S., Arcidiacono, S., Chikatamarla, S.S., Prasianakis, N.I., Gorban, A.N. & Karlin, I.V. 2007 Quasi-equilibrium lattice Boltzmann method. *Eur. Phys. J. B* **56**, 135–139.

Argrow, B.M. 1996 Computational analysis of dense gas shock tube flow. *Shock Waves* **6** (4), 241–248.

Borisov, A.A., Borisov, A.A., Kutateladze, S.S. & Nakoryakov, V.E. 1983 Rarefaction shock wave near the critical liquid–vapour point. *J. Fluid Mech.* **126**, 59–73.

Bres, G., Pérot, F. & Freed, D. 2009 Properties of the lattice Boltzmann method for acoustics. In *15th AIAA/CEAS Aeroacoustics Conference (30th AIAA Aeroacoustics Conference)*, p. 3395. American Institute of Aeronautics and Astronautics.

Chen, J., Liu, L., Liao, G., Zhang, F., Jiaqiang, E. & Tan, S. 2023 Design and off-design performance analysis of supercritical carbon dioxide Brayton cycles for gas turbine waste heat recovery. *Appl. Therm. Engng* **235**, 121295.

Chen, L., Kang, Q., Mu, Y., He, Y.-L. & Tao, W.-Q. 2014 A critical review of the pseudopotential multiphase lattice Boltzmann model: methods and applications. *Intl J. Heat Mass Transfer* **76**, 210–236.

Colonna, P., Medipati, C. & Mercier, B. 2026 Generation and measurement of rarefaction shock waves in dense vapors. https://doi.org/10.21203/rs.3.rs-8563199/v1

Colonna, P., Nannan, N.R., Guardone, A. & van der Stelt, T.P. 2009 On the computation of the fundamental derivative of gas dynamics using equations of state. *Fluid Phase Equilib.* **286** (1), 43–54.

Cook, A.W. & Cabot, W.H. 2004 A high-wavenumber viscosity for high-resolution numerical methods. *J. Comput. Phys.* **195** (2), 594–601.

Cramer, M.S., Whitlock, S.T. & Tarkenton, G.M. 1996 Transonic and boundary layer similarity laws in dense gases. *J. Fluids Engng* **118**, 481–485.

Dorschner, B., Bösch, F. & Karlin, I.V. 2018 Particles on demand for kinetic theory. *Phys. Rev. Lett.* **121** (13), 130602.

Duan, L., Zheng, Q., Jiang, Z. & Wang, J. 2021 Dense gas effect on small-scale structures of compressible isotropic turbulence. *Phys. Fluids* **33** (11), 115113.

Fang, W.-Z., Chen, L., Kang, Q.-J. & Tao, W.-Q. 2017 Lattice boltzmann modeling of pool boiling with large liquid-gas density ratio. *Intl J. Therm. Sci.* **114**, 172–183.

Fei, L., Yang, J., Chen, Y., Mo, H. & Luo, K.H. 2020 Mesoscopic simulation of three-dimensional pool boiling based on a phase-change cascaded lattice Boltzmann method. *Phys. Fluids* **32** (10), 103312.

Fiorina, B. & Lele, S.K. 2005 An artificial nonlinear diffusivity method for shock-capturing in supersonic reacting flows. In *Annual Research Briefs for the Center for Turbulence Research*, Stanford University.

Gallarini, S., Cozzi, F., Spinelli, A. & Guardone, A. 2021 Direct velocity measurements in high-temperature non-ideal vapor flows. *Exp. Fluids* **62**, 1–18.

Garnier, E., Adams, N. & Sagaut, P. 2009 *Large Eddy Simulation for Compressible Flows*. Springer Science & Business Media.

Giauque, A., Corre, C. & Menghetti, M. 2017 Direct numerical simulations of homogeneous isotropic turbulence in a dense gas. *J. Phys.: Conf. Ser.* **821**, 012017.

https://doi.org/10.1017/jfm.2026.11636 Published online by Cambridge University Press

GIAUQUE, A., CORRE, C. & VADROT, A. 2020 Direct numerical simulations of forced homogeneous isotropic turbulence in a dense gas. *J. Turbul.* **21** (3), 186–208.

GUARDONE, A., COLONNA, P., PINI, M. & SPINELLI, A. 2024 Nonideal compressible fluid dynamics of dense vapors and supercritical fluids. *Annu. Rev. Fluid Mech.* **56**, 241–269.

GUARDONE, A. & VIGEVANO, L. 2002 Roe linearization for the van der Waals gas. *J. Comput. Phys.* **175** (1), 50–78.

GUNAWAN, G., PERMANA, D.I. & SOETIKNO, P. 2023 Design and numerical simulation of radial inflow turbine of the regenerative Brayton cycle using supercritical carbon dioxide. *Results Engng* **17**, 100931.

GUNSTENSEN, A.K., ROTHMAN, D.H., ZALESKI, S. & ZANETTI, G. 1991 Lattice Boltzmann model of immiscible fluids. *Phys. Rev. A* **43** (8), 4320.

GUO, Z., ZHENG, C., SHI, B. & ZHAO, T.S. 2007 Thermal lattice Boltzmann equation for low Mach number flows: decoupling model. *Phys. Rev. E—Stat. Nonlinear Soft Matt. Phys.* **75** (3), 036704.

HÁZI, G. & MÁRKUS, A. 2008 Modeling heat transfer in supercritical fluid using the lattice Boltzmann method. *Phys. Rev. E* **77** (2), 026305.

HE, X., CHEN, S. & DOOLEN, G.D. 1998 A novel thermal model for the lattice Boltzmann method in incompressible limit. *J. Comput. Phys.* **146** (1), 282–300.

HE, X. & DOOLEN, G.D. 2002 Thermodynamic foundations of kinetic theory and lattice Boltzmann models for multiphase flows. *J. Stat. Phys.* **107**, 309–328.

HEAD, A.J., MICHELIS, T., BELTRAME, F., FUENTES-MONJAS, B., CASATI, E., DE SERVI, C. & COLONNA, P. 2022 Mach number estimation and pressure profile measurements of expanding dense organic vapors. In *International Seminar on Non-Ideal Compressible-Fluid Dynamics for Propulsion & Power*, pp. 229–238. Springer.

HOSSEINI, S.A. 2020 Development of a lattice Boltzmann-based numerical method for the simulation of reacting flows. PhD thesis, Université Paris-Saclay, Otto-von-Guericke-Universität Magdeburg.

HOSSEINI, S.A., BHADAURIA, A. & KARLIN, I.V. 2024 Probing double-distribution-function models in discrete-velocity Boltzmann methods for highly compressible flows: particles-on-demand realization. *Phys. Rev. E* **110** (4), 045313.

HOSSEINI, S.A., COREIXAS, C., DARABIHA, N. & THÉVENIN, D. 2019 Extensive analysis of the lattice Boltzmann method on shifted stencils. *Phys. Rev. E* **100** (6), 063301.

HOSSEINI, S.A., DARABIHA, N. & THÉVENIN, D. 2020 Compressibility in lattice Boltzmann on standard stencils: effects of deviation from reference temperature. *Phil. Trans. R. Soc. Lond. A* **378** (2175), 20190399.

HOSSEINI, S.A., DORSCHNER, B. & KARLIN, I.V. 2022*a* Towards a consistent lattice Boltzmann model for two-phase fluids. *J. Fluid Mech.* **953**, A4.

HOSSEINI, S.A., HUANG, F. & THÉVENIN, D. 2022*b* Lattice Boltzmann model for simulation of flow in intracranial aneurysms considering non-Newtonian effects. *Phys. Fluids* **34** (7), 073105.

HOSSEINI, S.A. & KARLIN, I.V. 2023 Lattice Boltzmann for non-ideal fluids: fundamentals and practice. *Phys. Rep.* **1030**, 1–137.

HUANG, R., WU, H. & ADAMS, N.A. 2021 Mesoscopic lattice Boltzmann modeling of the liquid–vapor phase transition. *Phys. Rev. Lett.* **126** (24), 244501.

IGRA, D. & TAKAYAMA, K. 2001 A study of shock wave loading on a cylindrical water column. *Rep. Inst. Fluid Sci. Tohoku Univ.* **13**, 19–36.

JACOBSEN, R.T., STEWART, R.B. & JAHANGIRI, M. 1986 Thermodynamic properties of nitrogen from the freezing line to 2000 K at pressures to 1000 MPa. *J. Phys. Chem. Ref. Data* **15** (2), 735–909.

KARLIN, I. & ASINARI, P. 2010 Factorization symmetry in the lattice Boltzmann method. *Phys. A: Stat. Mech. Applics* **389** (8), 1530–1548.

KARLIN, I. & HOSSEINI, S.A. 2026 Practical kinetic models for dense fluids. *Phys. Rev. Lett.* **136**, 104002.

KARLIN, I.V., BÖSCH, F. & CHIKATAMARLA, S.S. 2014 Gibbs' principle for the lattice-kinetic theory of fluid dynamics. *Phys. Rev. E* **90** (3), 031302.

KARLIN, I.V., SICHAU, D. & CHIKATAMARLA, S.S. 2013 Consistent two-population lattice Boltzmann model for thermal flows. *Phys. Rev. E* **88** (6), 063310.

KAWAI, S. 2019 Heated transcritical and unheated non-transcritical turbulent boundary layers at supercritical pressures. *J. Fluid Mech.* **865**, 563–601.

KOUREMENOS, D.A., ANTONOPOULOS, K.A. & KAKATSIOS, X.K. 1988 A correlation of the isentropic exponents of real gases. *Intl J. Heat Fluid Flow* **9** (4), 410–414.

LANDAU, L.D. & LIFSHITZ, E.M. 1987 *Fluid Mechanics*, vol. 6. Elsevier.

LETTIERI, C., YANG, D. & SPAKOVSZKY, Z. 2015 An investigation of condensation effects in supercritical carbon dioxide compressors. *J. Engng Gas Turbines Power* **137** (8), 082602.

https://doi.org/10.1017/jfm.2026.11636 Published online by Cambridge University Press

LI, Q., HE, Y.L., WANG, Y. & TAO, W.Q. 2007 Coupled double-distribution-function lattice Boltzmann method for the compressible Navier–Stokes equations. *Phys. Rev. E—Stat. Nonlinear Soft Matt. Phys.* **76** (5), 056705.

LI, Q., KANG, Q.J., FRANCOIS, M.M., HE, Y.L. & LUO, K.H. 2015 Lattice Boltzmann modeling of boiling heat transfer: The boiling curve and the effects of wettability. *Intl J. Heat Mass Transfer* **85**, 787–796.

LI, Q., LUO, K.H., HE, Y.L., GAO, Y.J. & TAO, W.Q. 2012 Coupling lattice Boltzmann model for simulation of thermal flows on standard lattices. *Phys. Rev. E—Stat. Nonlinear Soft Matt. Phys.* **85** (1), 016710.

LI, Q., LUO, K.H., KANG, Q.J., HE, Y.L., CHEN, Q. & LIU, Q. 2016 Lattice Boltzmann methods for multiphase flow and phase-change heat transfer. *Prog. Energy Combust. Sci.* **52**, 62–105.

LULLI, M., BIFERALE, L., FALCUCCI, G., SBRAGAGLIA, M. & SHAN, X. 2022*a* Mesoscale perspective on the tolman length. *Phys. Rev. E* **105** (1), 015301.

LULLI, M., BIFERALE, L., FALCUCCI, G., SBRAGAGLIA, M., YANG, D. & SHAN, X. 2022*b* Metastable and unstable dynamics in multi-phase lattice Boltzmann. arXiv preprint arXiv: 2212.07848.

LUO, K.H., FEI, L. & WANG, G. 2021 A unified lattice Boltzmann model and application to multiphase flows. *Phil. Trans. R. Soc. Lond. A* **379** (2208), 20200397.

MARTINEZ, D.O., MATTHAEUS, W.H., CHEN, S. & MONTGOMERY, D.C. 1994 Comparison of spectral method and lattice Boltzmann simulations of two-dimensional hydrodynamics. *Phys. Fluids* **6** (3), 1285–1298.

MAZLOOMI, A. *et al.* 2015 Entropic lattice Boltzmann method for multiphase flows. *Phys. Rev. Lett.* **114** (17), 174502.

MENG, J.C. & COLONIUS, T. 2015 Numerical simulations of the early stages of high-speed droplet breakup. *Shock Waves* **25** (4), 399–414.

NEDERSTIGT, P. & PECNIK, R. 2023 Generalised isentropic relations in thermodynamics. *Energies* **16** (5), 2281.

PECNIK, R. & PATEL, A. 2017 Scaling and modelling of turbulence in variable property channel flows. *J. Fluid Mech.* **823**, R1.

PEETERS, J.W.R., PECNIK, R., ROHDE, M., VAN DER HAGEN, T.H.J.J. & BOERSMA, B.J. 2016 Turbulence attenuation in simultaneously heated and cooled annular flows at supercritical pressure. *J. Fluid Mech.* **799**, 505–540.

PENG, Y., LIAO, W., LUO, L.-S. & WANG, L.-P. 2010 Comparison of the lattice Boltzmann and pseudo-spectral methods for decaying turbulence: low-order statistics. *Comput. Fluids* **39** (4), 568–591.

PINI, M. & DE SERVI, C. 2018 Entropy generation in laminar boundary layers of non-ideal fluid flows. In *International Seminar on Non-Ideal Compressible-Fluid Dynamics for Propulsion & Power*, pp. 104–117. Springer.

PRASIANAKIS, N.I. & KARLIN, I.V. 2007 Lattice Boltzmann method for thermal flow simulation on standard lattices. *Phys. Rev. E* **76** (1), 016702.

PRASIANAKIS, N.I. & KARLIN, I.V. 2008 Lattice Boltzmann method for simulation of compressible flows on standard lattices. *Phys. Rev. E* **78** (1), 016704.

QUIRK, J.J. & KARNI, S. 1996 On the dynamics of a shock–bubble interaction. *J. Fluid Mech.* **318**, 129–163.

RENARD, F., FENG, Y., BOUSSUGE, J.-F. & SAGAUT, P. 2021 Improved compressible hybrid lattice Boltzmann method on standard lattice for subsonic and supersonic flows. *Comput. Fluids* **219**, 104867.

REYHANIAN, E., DORSCHNER, B. & KARLIN, I. 2021 Kinetic simulations of compressible non-ideal fluids: from supercritical flows to phase-change and exotic behavior. *Computation* **9** (2), 13.

REYHANIAN, E., DORSCHNER, B. & KARLIN, I.V. 2020 Thermokinetic lattice Boltzmann model of nonideal fluids. *Phys. Rev. E* **102** (2), 020103.

RYKOV, V.A. 1975 A model kinetic equation for a gas with rotational degrees of freedom. *Fluid Dyn.* **10** (6), 959–966.

SAADAT, M.H., DORSCHNER, B. & KARLIN, I. 2021*a* Extended lattice Boltzmann model. *Entropy* **23** (4), 475.

SAADAT, M.H., HOSSEINI, S.A., DORSCHNER, B. & KARLIN, I.V. 2021*b* Extended lattice Boltzmann model for gas dynamics. *Phys. Fluids* **33** (4), 046104.

SAITO, S., DE ROSIS, A., FEI, L., LUO, K.H., EBIHARA, K.-I., KANEKO, A. & ABE, Y. 2021 Lattice Boltzmann modeling and simulation of forced-convection boiling on a cylinder. *Phys. Fluids* **33** (2), 023307.

SCIACOVELLI, L., CINNELLA, P. & GRASSO, F. 2017 Small-scale dynamics of dense gas compressible homogeneous isotropic turbulence. *J. Fluid Mech.* **825**, 515–549.

SHAN, X. & CHEN, H. 1993 Lattice Boltzmann model for simulating flows with multiple phases and components. *Phys. Rev. E* **47** (3), 1815.

https://doi.org/10.1017/jfm.2026.11636 Published online by Cambridge University Press

SIMEONI, G.G., BRYK, T., GORELLI, F.A., KRISCH, M., RUOCCO, G., SANTORO, M. & SCOPIGNO, T. 2010 The widom line as the crossover between liquid-like and gas-like behaviour in supercritical fluids. *Nat. Phys.* **6** (7), 503–507.

STRÄSSLE, R.M., HOSSEINI, S.A. & KARLIN, I.V. 2025 Consistent kinetic modeling of compressible flows with variable prandtl numbers: double-distribution quasi-equilibrium approach. arXiv preprint arXiv: 2510.04197.

SUCCI, S. 2001 *The Lattice Boltzmann Equation: for Fluid Dynamics and Beyond*. Oxford University Press.

SUCCI, S. & SUCCI, S. 2018 *The Lattice Boltzmann Equation: for Complex States of Flowing Matter*. Oxford University Press.

SWIFT, M.R., ORLANDINI, E., OSBORN, W.R. & YEOMANS, J.M. 1996 Lattice Boltzmann simulations of liquid-gas and binary fluid systems. *Phys. Rev. E* **54** (5), 5041.

THOMPSON, P.A. 1971 A fundamental derivative in gasdynamics. *Phys. Fluids* **14** (9), 1843–1849.

THOMPSON, P.A. & LAMBRAKIS, K.C. 1973 Negative shock waves. *J. Fluid Mech.* **60** (1), 187–208.

VADROT, A.ÉLIEN, GIAUQUE, A. & CORRE, C. 2021 Direct numerical simulations of temporal compressible mixing layers in a Bethe–Zel'dovich–Thompson dense gas: influence of the convective Mach number. *J. Fluid Mech.* **922**, A5.

VIENNE, L., GIAUQUE, A. & LÉVÊQUE, E. 2024 Hybrid lattice Boltzmann method for turbulent nonideal compressible fluid dynamics. *Phys. Fluids* **36** (11), 116138.

VIGGEN, E.M. 2011 Viscously damped acoustic waves with the lattice Boltzmann method. *Phil. Trans. R. Soc. Lond. A: Math. Phys. Engng Sci.* **369**, 2246–2254, 1944.

VIGGEN, E.M. 2014 Acoustic equations of state for simple lattice Boltzmann velocity sets. *Phys. Rev. E* **90** (1), 013310.

WISSOCQ, G., SAGAUT, P. & BOUSSUGE, J.-F. 2019 An extended spectral analysis of the lattice Boltzmann method: modal interactions and stability issues. *J. Comput. Phys.* **380**, 311–333.

ZEL'DOVICH, Y.B. 1946 On the possibility of rarefaction shock waves. *Zh. Eksp. Teor. Fiz.* **4** (16), 337–363.

ZOCCA, M., GUARDONE, A., CAMMI, G., COZZI, F. & SPINELLI, A. 2019 Experimental observation of oblique shock waves in steady non-ideal flows. *Exp. Fluids* **60**, 1–12.

https://doi.org/10.1017/jfm.2026.11636 Published online by Cambridge University Press